Markus Polanz, BSc

Helium Atom Scattering Measurements of the Sb(111) Surface including the Close Coupling Algorithm

MASTER THESIS

for obtaining the academic degree

Diplom-Ingenieur

Master's Programme of
Technical Physics

TU Graz
Graz University of Technology

Graz University of Technology

Supervisor:
Univ.-Prof. Mag. Dr.rer.nat Wolfgang E. Ernst
Institute of Experimental Physics

Graz, January 2014

Acknowledgement

First of all I want to thank my supervisor Prof. W. E. Ernst for his faith in me. Without him this master thesis would not have been possible.

I am deeply grateful to my colleagues Michael Mayrhofer-Reinhartshuber, Patrick Kraus and Anton Tamtögl for their friendliness and patience. The practical work in the helium atom scattering laboratory with them was a pleasure. I very much appreciated the very good advice and help on the practical and theoretical projects.

Furthermore, I would like to thank all members of the Institute of Experimental Physics for their cooperation. Without the skills of the staff from the mechanical and electrical fraction some projects would not have been possible. I also would like to thank the charming secretaries.

The biggest thanks of all go to my parents Ewald and Angelika and to my little sister Silvia. They are the most important people in my life. Without their support and trust during my whole life I would not be where I am now. Moreover, I would like to thank all my friends I met in Graz. They brighten up my life every day.

EIDESSTATTLICHE ERKLÄRUNG

Ich erkläre an Eides statt, dass ich die vorliegende Arbeit selbstständig verfasst, andere als die angegebenen Quellen/Hilfsmittel nicht benutzt, und die den benutzten Quellen wörtlich und inhaltlich entnommene Stellen als solche kenntlich gemacht habe.

Graz, am …………………………   …………………………………………………..
                                                                                (Unterschrift)

STATUTORY DECLARATION

I declare that I have authored this thesis independently, that I have not used other than the declared sources / resources, and that I have explicitly marked all material which has been quoted either literally or by content from the used sources.

……………………………   …………………………………………………..
        date   (signature)

Abstract

The recently discovered topological insulators are the object of current research. Here, the semimetals Sb and Bi are an important part of a number of compounds. Since the crystal surface of these elements behaves differently from the crystal itself, the investigation of the surface properties and structure of these semimetals is an interesting research field. From the view of atom scattering, helium atoms are suited the best, because of their high surface sensitivity. This Master thesis is concerned exclusively with elastic helium atom scattering processes on Sb(111) surfaces. Not only the structure of the crystal surface but also the Debye temperature of the surface can be determined. Inelastic scattering processes of helium atoms on the crystal surface are also of interest. Through energy loss or gain of the scattered helium atoms, surface phonons will be created or annihilated. Therefore it is possible to determine the phonon dispersion relation experimentally.

The elastic scattering intensities are calculated numerically with approximate methods. An exact method, which is presented in this thesis, is the Close Coupling algorithm. Here the time independent Schrödinger equation for a certain particle-surface interaction potential is solved. Not only the surface corrugation, but also resonance effects can be calculated with this method.

Kurzfassung

Die erst kürzlich entdeckten topologischen Isolatoren sind Gegenstand aktueller Forschung. Dabei sind die Halbmetalle Sb und Bi wichtiger Bestandteil zahlreicher Verbindungen. Da sich die Kristalloberfläche dieser Elemente anders verhält als der Kristall selbst, ist die Untersuchung der Oberflächeneigenschaften und Oberflächenstruktur dieser Halbmetalle ein interessantes Forschungsgebiet. Durch die hohe Oberflächensensibilität sind Heliumatome vom Standpunkt der Atomstreuung aus am besten geeignet. Diese Diplomarbeit beschäftigt sich ausschließlich mit elastischen Heliumatom Streuprozessen an Sb(111) Oberflächen. Damit kann nicht nur die Struktur der Kristalloberfläche sondern auch die Debye Temperatur der Oberfläche bestimmt werden. Daneben sind auch die inelastischen Streuprozesse der Heliumatome auf Kristalloberflächen von Interesse. Durch den Energieverlust oder -gewinn der gestreuten Helium Atome werden Oberflächenphononen erzeugt oder vernichtet. Dadurch wird es möglich die Phononendispersionsrelation experimentell zu bestimmen.

Die elastischen Streuintensitäten werden mit Näherungsmethoden numerisch berechnet. Eine exakte Methode, die in dieser Arbeit vorgestellt wird, ist der Close Coupling Algorithmus. Hier wird die zeitunabhängige Schrödingergleichung für ein spezielles Teilchen-Oberfläche Interaktionspotential gelöst. Nicht nur die Oberflächenrauhigkeit sondern auch Resonanzeffekte können mit dieser Methode berechnet werden.

Contents

List of Figures

List of Tables

1. Introduction

The helium atom scattering (HAS) method is the usual choice for crystal surface investigations because of the high surface sensitivity of the helium atoms. In contrast to other particles, helium atoms are directly scattered from the surface electron density. In this case only the topmost layer contributes to the scattering processes. This makes it possible to get only information about the crystal surface. The theoretical background of the HAS technique is given in chapter 2.

The measurements are done with a HAS apparatus, which was bought in 2007 from the Free University of Berlin and remounted till 2009.[8] The main fact of this type of HAS machines is that the angle enclosed by the source arm and the detector arm is fixed and the position of the sample, which is placed on a sample holder, can be changed by a six axes manipulator. The helium beam is generated by a supersonic expansion through a nozzle. This yields a monochromatic helium beam with a high intensity and a small energy spread. Several improvements on the HAS apparatus were done during the work of this thesis. They are described in detail in chapter 3.[3]

In the case of the elastic HAS process, diffraction peaks of different orders occur during the angular scan measurements. Here the scattered intensity is recorded as a function of the incident (polar) angle θ_i. Out of the angular positions and heights, the crystal surface structure and the surface Debye temperature respectively are obtained. In inelastic HAS processes surface phonons are either created or annihilated. Thus, it is possible to measure the phonon dispersion relation. This is done by the Pseudo-Random-Chopper technique for time-of-flight (TOF) measurements. In chapter 4 is shown, how the elastic scattering measurements are performed.[5,9]

Until now the elastic scattering intensities were calculated by approximate methods, such as the Eikonal-approximation or the GR-method. The Close Coupling (CC) algorithm, which was used within the work of this thesis, is an exact method. As computer processors have become faster, this method is increasingly of interest. Not only elastic scattering intensities can be calculated, but also resonance effects of helium atoms on the surface can be computed.[10]

These measurements and calculations were recently done for the Bi(111) crystal surface. In this thesis, the Sb(111) crystal surface, which has quite similar structures and properties as Bi(111), is investigated. Chapter 5 deals with the structure

and properties of the Sb(111) crystal surface.[11–14]

The thesis focusses mainly on the elastic HAS measurements on Sb(111) crystal surfaces, which are detailed in the chapter Results and Discussion. Also the lattice constant of Sb(111) was determined out of angular scans in the $< 10 >$ scattering direction. Finally, two CC-programs were tested on GR-method calculations from García.[15] Manuals for all programs used in this thesis can be found in the Appendix.

2. Theoretical Background

The theoretical aspects of the helium atom scattering (HAS) method are covered in this chapter. First of all, the mathematical description of crystals and crystal surfaces is shown. Moreover, important HAS processes with a special emphasis on the elastic and inelastic scattering of helium atoms are explained. Also the generation of the helium beam with a supersonic expansion and the time-of-flight (TOF) method are described in this section. Subsequently, different approximate methods are presented to calculate the elastic scattering intensities. Since there are many different particle-surface interaction potential models, the most important ones used in this thesis are described in this section. The Close Coupling (CC) algorithm, which is an important part of this thesis, is described in the next section. Finally, the powerful finite-element-method (FEM) is presented, which was used to calculate the temperature distribution in matter out of the heat equation numerically.

2.1. Crystal Surface Characterization

In this section the mathematical notation for crystals and crystal surfaces used in this thesis is described. The works of Hofmann[1] or Oura et al[16] serve as an introduction to surface physics. More details about solid state physics is given in Kittel's work.[17]

2.1.1. Description of Crystals

A crystal is a three-dimensional periodic arrangement of atoms. Therefore, it can be described by repetition of identical units. From the mathematical point of view a crystal lattice, consisting of lattice points, is used. It describes the arrangement of atoms in the crystal as well as the symmetry of the crystal. The three vectors $\vec{a}_1$, $\vec{a}_2$ and $\vec{a}_3$ form the translation vector:

$$\vec{R} = h\vec{a}_1 + k\vec{a}_2 + l\vec{a}_3 \tag{2.1}$$

where h, k and l are integer numbers. The three primitive translation vectors $\vec{a}_1$, $\vec{a}_2$ and $\vec{a}_3$ build a parallelepiped that encloses the smallest possible volume

in the crystal. By repetition of this primitive unit cell the whole space is filled completely. The vectors $\vec{R}$ also define the 14 distinct lattice types in 3D (Bravais lattices). Starting from a point $\vec{r}$ one can get to a point $\vec{r'}$ by a translation $\vec{R}$, from where the crystal looks exactly the same:

$$\vec{r'} = \vec{r} + \vec{R} \tag{2.2}$$

To get the real crystal structure, a basis consisting of a group of atoms is placed on each lattice point.[1,16,17]

Reciprocal Lattices in 3D

By Fourier transformation one gets from the real space into the reciprocal space. In this space the lattices are also Bravais lattices. They are defined by a set of reciprocal lattice vectors $\vec{G}$ that describe plane waves. The periodicity of these waves is given by the Bravais lattice. The relation

$$\exp(i\vec{G}\vec{R}) = 1 \tag{2.3}$$

between the points $\vec{R}$ of the Bravais lattice and the vectors $\vec{G}$ is fulfilled. The vectors $\vec{G}$ are defined in a similar way as the real translation vectors $\vec{R}$:

$$\vec{G} = h\vec{b_1} + k\vec{b_2} + l\vec{b_3} \tag{2.4}$$

where h, k and l are again integer numbers. The primitive reciprocal lattice vectors $\vec{b_1}$, $\vec{b_2}$ and $\vec{b_3}$ that define the lattice are yielded in the following way:

$$\vec{b_1} = 2\pi \frac{\vec{a_2} \times \vec{a_3}}{\vec{a_1}(\vec{a_2} \times \vec{a_3})}, \vec{b_2} = 2\pi \frac{\vec{a_3} \times \vec{a_1}}{\vec{a_1}(\vec{a_2} \times \vec{a_3})}, \vec{b_3} = 2\pi \frac{\vec{a_1} \times \vec{a_2}}{\vec{a_1}(\vec{a_2} \times \vec{a_3})} \tag{2.5}$$

A simple relation between the vectors $\vec{a_i}$ and $\vec{b_j}$ is:

$$\vec{a_i}\vec{b_j} = 2\pi\delta_{ij} \tag{2.6}$$

The most important aspect of the reciprocal space is that problems from solid state physics are written in an easier way because of utilizing the crystal symmetry.[1,16,17]

2.1.2. Description of Crystal Surfaces

In two dimensions the crystal symmetry is broken perpendicular to the surface. To distinguish the different crystal planes they are labeled with Miller-indices. They are determined by the following steps:

- Find the interceptions of the specific plane with the axes in terms of the lattice constant.

- Take the reciprocals of the yielding numbers.

- Calculate the least common multiple of the three denominators.

- Multiply the three numbers of the 2nd step with the previous result.

The resulting numbers are written in parantheses and represent the specific crystal plane. If a plane does not intercept with an axes the number of this index is zero (e.g. (110)). Equivalent sets of planes are characterized in braces (e.g. {100}). Directions are given in square brackets (e.g. [111]).[17]
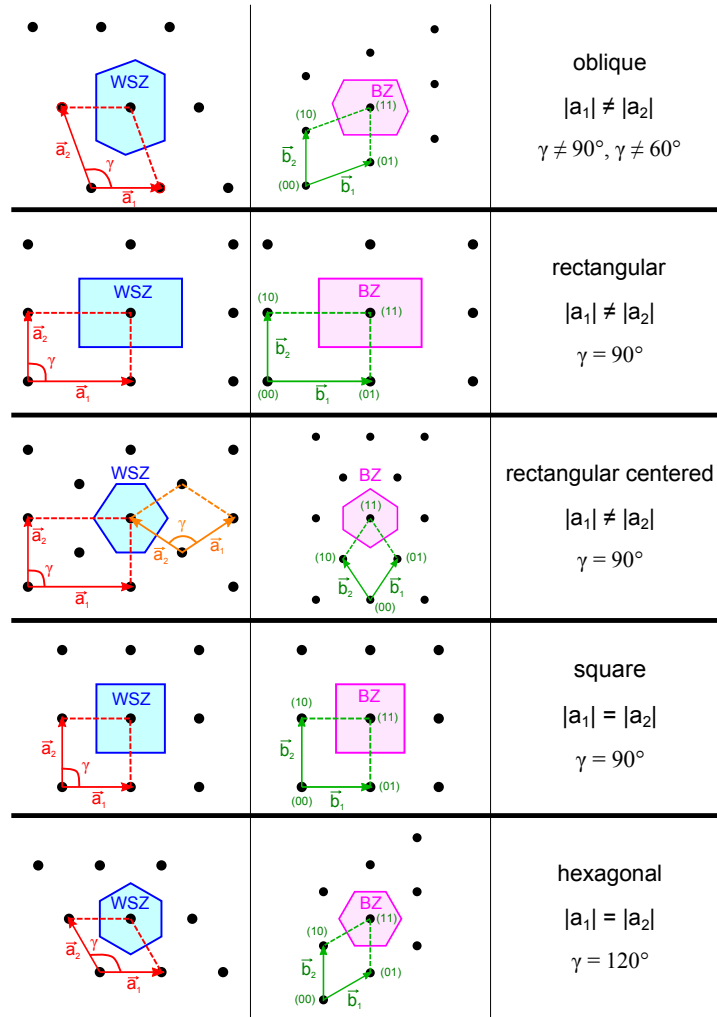
Figure 2.1.: The 5 bravais lattice types in 2D. The first column corresponds to the real and the second column to the reciprocal space. The Wigner-Seitz cell (WSZ) and the first Brillouin zone (BZ) are drawn.

The crystal surface is a two-dimensional structure. Due to the finite thickness, the surface structure is three-dimensional, but the symmetry operations are two-

dimensional. The crystal surface lattice is described in a similar way as for the bulk case. The only difference is, that normally two vectors are needed to form the translation vector $\vec{R}$ on the surface:

$$\vec{R} = h\vec{a}_1 + k\vec{a}_2 \tag{2.7}$$

h and k are integer numbers. The remaining third vector can be thought of as the unity vector $\vec{n}$ standing normal to the surface and pointing in the positive z-direction. The primitive translation vectors $\vec{a}_1$ and $\vec{a}_2$ form a parallelogram. This primitive unit cell encloses the smallest area in the surface lattice.[1]

The different lattice types in two dimensions are summarized in the so called Bravais lattices, which are distinct. In two dimensions only 5 Bravais lattices are known. They are shown in fig. 2.1 with their properties. Note that in the centered rectangular case, the primitive cell is non-rectangular.[16,18]

Reciprocal Lattices in 2D

Diffraction experiments are described in the reciprocal space. The two-dimensional reciprocal lattice is defined in the same way as the three-dimensional one, except that the 3rd basis-vector is replaced with the surface normal vector $\vec{n}$. The primitive translation vectors in reciprocal space $\vec{b}_1$ and $\vec{b}_2$ are constructed with the primitive translation vectors in real space $\vec{a}_1$ and $\vec{a}_2$ as follows:

$$\vec{b}_1 = 2\pi \frac{\vec{a}_2 \times \vec{n}}{|\vec{a}_1 \times \vec{a}_2|}, \vec{b}_2 = 2\pi \frac{\vec{n} \times \vec{a}_1}{|\vec{a}_1 \times \vec{a}_2|} \tag{2.8}$$

Here $\vec{n}$ is the unit vector normal to the surface. A general translation vector of the reciprocal lattice is defined by:

$$\vec{G}_{hk} = h\vec{b}_1 + k\vec{b}_2 \tag{2.9}$$

where h and k are integer numbers. From a given point in the reciprocal lattice, every point can be reached by a reciprocal lattice vector $\vec{G}_{hk}$.[1,16,18]

In fig. 2.1 the reciprocal lattices of the 5 Bravais lattices are shown.

2.1.3. The Wigner Seitz Cell and the First Brillouin Zone

There is a general way to construct a primitive unit cell in real space from Wigner and Seitz. The instruction for this Wigner-Seitz Cell consists of the following three steps:

- From an arbitrarily chosen lattice point, lines are drawn to the closest neighboring lattice points.

- Perpendicular lines (planes in 3D) are drawn at the midpoint of every line.

- The Wigner-Seitz Cell is then defined by the smallest area (volume in 3D) that is enclosed by these perpendicular lines (planes in 3D).

A primitive unit cell contains exactly one lattice point and shows the crystal symmetry. In the reciprocal space the Wigner-Seitz cell is called the first Brillouin Zone and the enclosing lines (planes in 3D) build the Brillouin zone boundary. It is the usual choice for the description of phonon or electron band structures of crystals and crystal surfaces.[17]
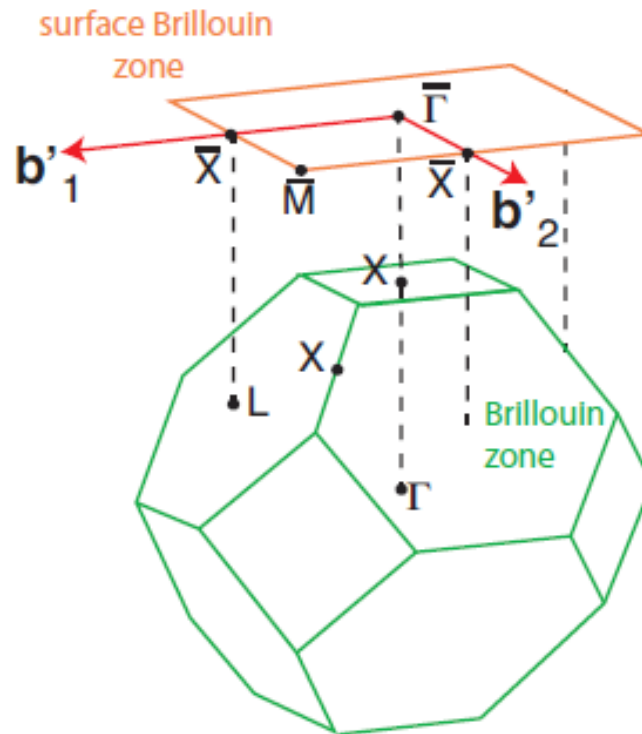
Figure 2.2.: Bulk Brillouin zone of a fcc lattice. The surface Brillouin zone for fcc(001) is obtained by projection onto the (001) surface.[1]

A widely used indication of the symmetry points and directions is the BSW (Bouckaert-Smoluchowski-Wigner) notation, where the center of the Brillouin zone is indicated by Γ. The Surface Brillouin Zone yields out of a projection from points of the three dimensional Brillouin zone onto the two dimensional Brillouin zone as can be seen in fig. 2.2. For a better distinction the symmetry points of the surface are indicated with a bar.[16–18]

2.2. The Helium Atom Scattering (HAS) Method

Atomic and molecular beam experiments have some advantages over other surface investigation techniques. Beside helium other particles like Ne, H_2, D_2, HD, H and D have been used so far. Helium is the usual choice for surface studies because of its high surface sensitivity. Also helium has advantages over other particles that were used.

Energies of the atomic or molecular beam in the range of (5-300) meV are used in diffraction experiments. At these energies no surface penetration occurs. Thus the surface sensivity is very high. Helium is a noble gas and is electrically and magnetically inert. Therefore it does not make any reasonable interactions with the sample. Furthermore, the sample surface is not destroyed by the low impact energies of the helium atoms. That is why the HAS technique is a nondestructive method. Also no electronic transitions are yielded from energy that is gained from thermal collisions with other particles. Helium has a closed shell (spherical shape) and thus has only three translational degrees of freedom. Helium is the lightest noble gas and hence the elastic part of the scattering process is enhanced. In comparison to many other particles used in atomic and molecular beam experiments, helium is smaller. Thus the interaction of the helium atom with the sample is shorter and more localized. It is possible to resolve sharp diffraction peaks and small changes in the velocity of the scattered beam with HAS. There are also certain disadvantages by using a helium beam. In contrast to particles like electrons, the He-atoms are big and slow. This leads to a slow variation of the lattice displacement in time and space during the interaction. An effective cutoff then occurs, which means that at certain wavevector and frequency values it is more difficult to create or annihilate phonons. If the interaction is more impulsive between the helium atoms and the surface, this cutoff is not a big problem, but the surface sensitivity then gets lower, because the particles penetrate deeper into the sample.[3,5]

In this section the creation and properties of the helium beam generated with a supersonic expansion are shown. Also a brief description of the highly used time-of-flight (TOF) method in atomic and molecular beam experiments is given. The main part consists of the occuring HAS processes on the surface. Two of them, the elastic and inelastic scattering processes, are described in more detail.

2.2.1. Generation of the Helium Beam

The generation of the helium beam, which is used for the HAS experiments, is done by a Free Jet Source, which is drawn schematically in fig. 2.3. With the principle of the supersonic expansion, the helium gas is expanded from a high

pressure region p_0 through a nozzle with a diameter of 10 μm into a vacuum chamber with low pressure p_a. With increasing distance x from the nozzle, the density of the particles $n(x)$ decreases:

$$n(x) \propto \frac{d}{x^2} \tag{2.10}$$

Close to the nozzle the flow region is continuous, where the expanded gas particles still interact with each other because of the high density. The quitting surface separates this region from the free molecular flow region, where there are no collisions of the particles. At sufficiently large ratios p_0/p_a the gas flow reaches sonic speed at the outside of the nozzle. The high pressure is in the region of $p_0 = (30-60)$ bar and the low pressure around $p_a \leq 1{\cdot}10^{-6}$ mbar. The parameters are chosen such that the mean free paths λ of the particles are smaller than the diameter d of the nozzle. The interactions between the particles become more important than the interactions of the particles with the surrounding region. The expansion can be assumed in this case as adiabatic and isentropic. A part of this expansion is selected by the skimmer, which is built of a conically shaped aperture. The whole internal energy is transformed to translational kinetic energy. The enthalpy at temperature T_0 and thus the energy of a particle in the helium beam is given by:

$$h(T_0) = \frac{\gamma}{\gamma - 1} k_B T_0 = \frac{5}{2} k_B T_0 \tag{2.11}$$

k_B is Boltzmanns constant, T_0 the initial nozzle temperature and γ the adiabatic index. For helium γ is $\frac{5}{3}$ because it has three translational degrees of freedom. In the case of an adiabatic expansion, the conservation of the sum of the kinetic energy of directed mass flow and the molar enthalpy h is given by:

$$h + \frac{mv^2}{2} = const \tag{2.12}$$

m is the mass of the particle and v the average velocity. Out of this relation the maximum flow velocity can be calculated:

$$v_{max} = \sqrt{\frac{2h(T_0)}{m}} \tag{2.13}$$

When the mean free path becomes larger, there is nearly no interaction between the atoms or molecules anymore. A part of the beam in this region travels in a very well defined direction chosen by the skimmer that is applied in the free molecular region. The main advantages of this creation method is the high intensity of the helium beam and the narrow velocity distribution f(v).[3,5,19]
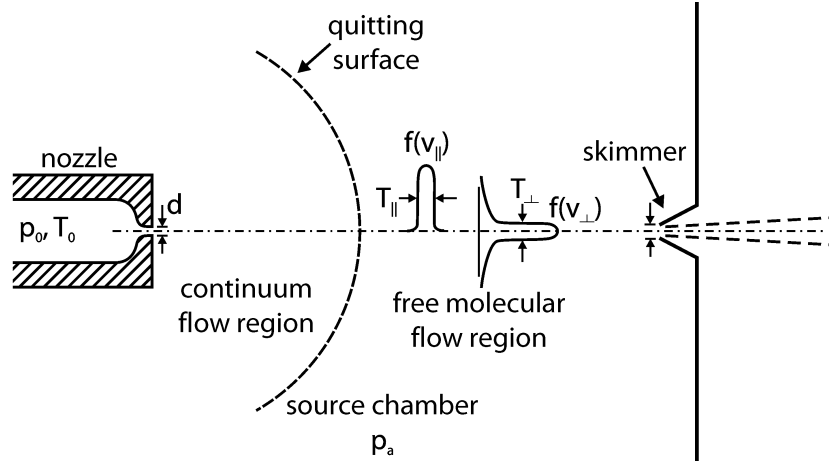
Figure 2.3.: Schematic drawing of a free jet source. The quitting surface separates the continuous flow region from the free molecular flow region.[2]

The intensity of a free jet beam is given by the intensity along the centreline going from the nozzle to the skimmer. The intensity at the skimmer is easier to predict than the intensity behind the skimmer. The intensity per solid angle I_0 of an ideal beam is:

$$I_0 = \frac{\kappa \dot{N}}{\pi} \tag{2.14}$$

κ is a peaking factor proposed by Beijerinck and Verster[20] and $\dot{N}$ is the nozzle flow rate in molecules/s. It can be written as:

$$\dot{N} = F(\gamma) n_0 \sqrt{\frac{2 k_B T_0}{m}} \left(\frac{\pi d^2}{4} \right) \tag{2.15}$$

where $F(\gamma)$ is a function of the adiabatic index γ:

$$F(\gamma) = \left(\frac{\gamma}{\gamma + 1} \right)^{\frac{1}{2}} \left(\frac{2}{\gamma + 1} \right)^{\frac{1}{\gamma - 1}} \tag{2.16}$$

k_B is Boltzmanns constant, m the helium atom mass and n_0 is the gas density, which can be expressed by the ideal gas law:

$$p_0 V = N k_B T_0 \Rightarrow n_0 = \frac{N}{V} = \frac{p}{k_B T_0} \tag{2.17}$$

This yields:

$$\dot{N} = F(\gamma) \frac{\pi}{4} \sqrt{\frac{2}{m k_B T_0}} p_0 d^2 \tag{2.18}$$

The intensity of the helium beam I_0 depends on the initial nozzle temperature T_0 in the following way:

$$I_0 \propto \frac{1}{\sqrt{T_0}} \tag{2.19}$$

This means that it is possible to measure higher order diffraction peaks by increasing the nozzle temperature.[5,20]

In the absence of the skimmer and the separating wall between the source chamber and the chamber after the skimmer the ideal case is present. Two main processes decrease the intensity of the helium beam when the ideal case is not considered. Some particles hit the wall and thus can not reach the target. Moreover, reflected particles disturb the flight of other particles through the skimmer. An approximation for the intensity I at the target for a diffusion pumped system is given by David R. Miller:[2]

$$I \approx I_0 \left(1 - \exp \left(-S^2 \left(\frac{r}{x_q} \right)^2 \left(\frac{x_d}{x_d - x_s} \right)^2 \right) \right) \tag{2.20}$$

r is the radius of the skimmer hole, x_q, x_d and x_s are the distances of the quitting surface, the target/detector and the skimmer from the nozzle respectively. The continuum speed ratio at the quitting surface is given by S, the ratio of the mean velocity and the thermal spread in velocities. If the conditions $S > 5$, $x_s > x_q$ and $x_d - x_s >> r$ are fulfilled and the background scattering can be neglected, then equ. 2.20 is valid.[2,3,5,19-21]

2.2.2. Time-Of-Flight (TOF) Measurements

In atomic and molecular beam experiments the time-of-flight (TOF) measurement method is an important tool. Basically the energies of the particles in the beam are determined by the following very simple physical principle. The particles are flying a certain distance of length l from the source to the detector. By measuring the traveling time t of the particles, the velocity v is obtained with $v = \frac{l}{t}$.[3,5]

Usually the helium nozzle is emitting particles continuously. Because the particles with different speeds and different initial times overlap each other this would cause a continuous signal at the detector. Therefore the starting time of the particles at the nozzle has to be defined exactly. Thus a chopper disc is placed at the beginning of the path which chops the continuous helium beam into particle bunches. For this the disc has well defined slits and rotates with a certain rotation speed in the vacuum chamber. Further slits are used to trigger an electrooptical light barrier system. In this way starting points in time as well as in space are determined with the chopper disc for the measurement of the flight time t and the flight path l.[3,5]

At the end of the flight path the particles reach the detector. The flight times t through the vacuum chambers are different since the particles have different velocities v. Usually particle packets are created with the chopper disc at the nozzle and have a certain velocity distribution. This is the reason why the packets are getting broader for longer flight times. On their way to the detector, atoms and molecules can loose or gain energy which leads to a time difference, which is proportional to the energy transfer. Out of the measured flight time distribution g(t) the velocity distribution f(v) and energy distribution f(E) of the particles can be obtained. If this process is repeated several times the signal-to-noise ratio (SNR) is optimized. Further details on this topic is given by M. Mayrhofer-Reinhartshuber in his Master thesis including the very important Pseudo-Random-Chopper technique.[5,21,22]

2.2.3. Elastic HAS from Surfaces

Every particle can be treated as a wave with a certain wavelength, which was shown by de Broglie in 1924. In HAS experiments it has to be smaller than the surface atom distance. The relation between the de-Broglie wavelength λ_i and the incident energy E_i is as follows:

$$\lambda_i = \frac{h}{p_i} = \frac{h}{mv_i} = \frac{h}{\sqrt{2mE_i}} \tag{2.21}$$

p_i and v_i are the incident momentum and velocity respectively. h is the Planck's constant and m the mass of the helium particle. The average translational energy E_i corresponds to the enthalpy given by equ. 2.11:

$$E_i = \frac{mv_i^2}{2} = \frac{5}{2}k_B T_N \tag{2.22}$$

k_B is the Boltzmann constant and T_N the nozzle temperature of the gas. Furthermore the initial helium beam energy E_i is related to the incident wavevector k_i of the incoming particle. The quantity wavevector, which is presented in the reciprocal space, is the most important parameter to describe scattering experiments:

$$E_i = \frac{\hbar^2 k_i^2}{2m} \tag{2.23}$$

The direction of the incident wavevector $\vec{k}_i$ is the same as in real space and characterized by its length:

$$k_i = \frac{2\pi}{\lambda_i} \tag{2.24}$$

In diffraction experiments it is helpful to describe this wavevector by a lateral component $\vec{K}_i$ and a perpendicular component k_{iz} that stands normal to the surface (see fig. 2.4):

$$\vec{k}_i = (\vec{K}_i, k_{iz}) \tag{2.25}$$

with

$$|\vec{K}_i| = k_i \sin(\Theta_i), \, k_{iz} = k_i \cos(\Theta_i) \tag{2.26}$$
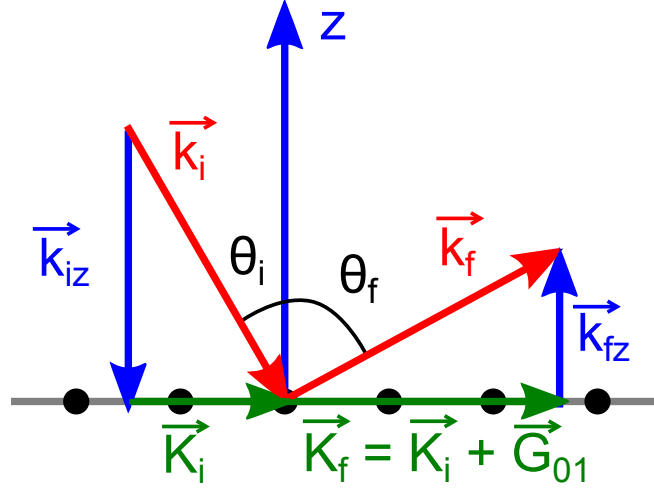
Figure 2.4.: Elastic in-plane scattering of the helium particles from the sample surface. The incident wavevector $\vec{k}_i$ consists of a lateral component $\vec{K}_i$ and a component k_{iz} normal to the surface in z-direction.

In elastic HAS processes the energy of the helium beam is conserved, which means that the difference of the energy before (E_i) and after (E_f) the particle is scattered on the surface is zero. The energy conservation leads to the fact that the length of the incident ($\vec{k}_i$) and the final ($\vec{k}_f$) wavevector is also conserved:

$$E_i = E_f \Rightarrow k_i = k_f \tag{2.27}$$

For an incident wavevector $\vec{k}_i$ diffraction peaks of several orders are observed. In the case of the crystal surface this is described by the Laue condition in two dimensions:

$$\vec{K}_i - \vec{K}_f = n\vec{G} \tag{2.28}$$

n is an integer number and $\vec{G}$ a reciprocal surface vector. This condition results from the conservation of the lateral part of the momentum. For very surface

sensitive beams (e.g. helium beams), there is a broken symmetry normal to the surface. Therefore the reciprocal lattice points along the z axis are becoming lattice rods. One distinguishes between in-plane and out-of-plane diffraction. In the case of the in-plane scattering the incident beam, diffracted beam and surface normal of the sample are in the same plane. When the helium beam is diffracted out-of-plane the projection of the diffracted beam onto the surface and the plane are enclosing an angle (azimuth angle). In this thesis only in-plane diffraction processes can be measured with the HAS apparatus.[5,23]

The Laue condition for the observation of diffraction peaks can be visualized by the Ewald construction: In three dimensions an Ewald sphere with radius k_i is drawn in the reciprocal space. At the intersections of the sphere and the reciprocal lattice points, diffraction peaks appear. In two dimensions the Ewald sphere is reduced to an Ewald circle. Here the intersections of the Ewald circle with the lattice rods lead to observable diffraction peaks (see fig. 2.5).[3]
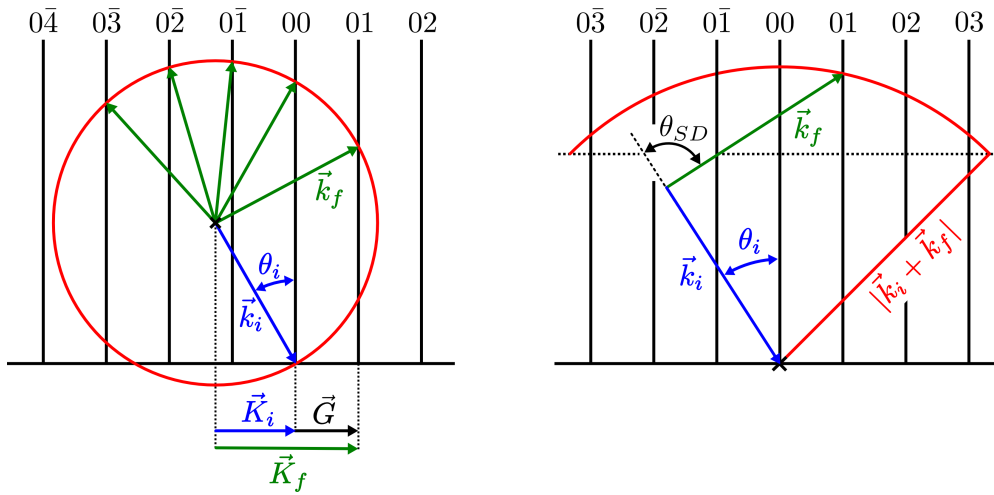
Figure 2.5.: Ewald Sphere construction in two dimensions. The symmetry perpendicular to the surface is broken and thus the points become lattice rods. The directions of the diffracted beams are given by the intersections of the circle with the lattice rods (left). In the case of our HAS apparatus with a fixed surface-detector angle Θ_{SD} things are a little bit different (right).[3]

To calculate the diffraction peak positions, the beam parameters and the lattice type of the sample have to be known. The sum of the incident (Θ_i) and the final angle (Θ_f) is fixed and therefore both angles cannot be changed independently.

$$\Theta_{SD} = \Theta_i + \Theta_f \tag{2.29}$$

Θ_{SD} is the angle between the source arm and the detector arm. The lateral components of the final wavevector can be written as:

$$|\vec{K}_f| = k_f \sin(\Theta_f) = k_i \sin(\Theta_f) \tag{2.30}$$

This results from the energy conservation given in equ. 2.27. The Laue condition given by equ. 2.28 for two dimensions is written as follows:

$$\sin(\Theta_f) = \sin(\Theta_i) + \frac{G}{k_i} \tag{2.31}$$

with equ. 2.26 and equ. 2.30. Plugging in $\Theta_f = \Theta_{SD} - \Theta_i$ leads to:

$$\sin(\Theta_{SD} - \Theta_i) - \sin(\Theta_i) = \frac{G}{k_i} \tag{2.32}$$

With the trigonometric relation $\sin(x) - \sin(y) = 2\sin(\frac{x-y}{2})\cos(\frac{x+y}{2})$ it is possible to obtain the angles Θ_i where diffraction peaks are observed:

$$\Theta_i = \frac{\Theta_{SD}}{2} - \arcsin\left(\frac{G}{2k_i}\sec\left(\frac{\Theta_{SD}}{2}\right)\right) \tag{2.33}$$

There is a final set $\vec{F}$, which represents a number of reciprocal lattice vectors, for which the appearance of diffraction peaks is restricted. The condition for this is:

$$k_{\vec{F}z}^2 = k_i^2 - (\vec{K}_i + \vec{F})^2 > 0 \tag{2.34}$$

$k_{\vec{F}z}$ is the component normal to the surface of the final wavevector. It can also be seen in the Ewald constructions shown in fig. 2.5. Because of the size of the incident wavelength, the size of the circle is finite and therefore only a certain number of reciprocal lattice rods are intersected.[3,5]

2.2.4. Inelastic HAS from Surfaces

In contrast to elastic scattering processes the difference between the final energy E_f and the incident energy E_i of the helium atoms is not zero for the inelastic diffraction case. The interaction of the helium particles with the crystal surface causes an energy change ΔE. The conservation of energy then is written as:

$$E_f = E_i + \Delta E \tag{2.35}$$

The main process which occurs through the particle-surface interaction is the creation or annihilation of phonons. These are collective vibrations of atoms in the crystal. As an assumption in one interaction process only one phonon is created or annihilated, which is called a single phonon event. Related to the phonon frequency ν the energy exchange can be written as:

$$\Delta E = h\nu \tag{2.36}$$

Similarly to the observation of in-plane elastic scattering events only atomic vibrations which are polarized in the sagittal plane can be investigated on the surface. This plane is defined by the surface normal of the crystal and the direction of the incident wavevector of the incoming helium particle. That is why horizontally polarized phonons are not observed by the HAS. Taking the surface phonon wavevector $\vec{Q}$, which is in the first surface Brillouin zone, into account the conservation of the lateral components of the momentum is given by:

$$\Delta\vec{K} = \vec{K}_i - \vec{K}_f = \vec{G} + \vec{Q} \tag{2.37}$$

$\vec{K}_i$ and $\vec{K}_f$ are lateral components of the incident and the final wavevector respectively. $\vec{G}$ is a reciprocal surface lattice vector. If the phonon energies are measured for wavelengths ranging from zero to the border of the first surface Brillouin zone, the surface phonon dispersion relation is obtained. This relation is given by the fact that the phonon energy is a function of the phonon wavevector. By varying the incident angle Θ_i the phonon wavevector of the created or annihilated phonon is changed. If the energy change ΔE is measured and the equations 2.35 and 2.37 are used, the phonon wavevector is determined. It is assumed that the reciprocal lattice vector $\vec{G}$ is equal to zero:[3,5]

$$|\vec{Q}| = |\Delta\vec{K}| = k_f\sin(\Theta_f) - k_i\sin(\Theta_i) \tag{2.38}$$

$$|\vec{Q}| = \sqrt{k_i^2 \pm \frac{2m}{\hbar^2}}\sin(\Theta_f) - k_i\sin(\Theta_i) \tag{2.39}$$

2.3. Calculation of Elastic Scattering Intensities

Helium atoms are scattered from crystal surfaces in a different way than electrons, neutrons or X-rays. Unlike the last-named particles, which are scattered by the ion cores at the surface, helium atoms are scattered by the electron density at the surface. Hence out of measured diffraction peak intensities, it is possible to determine the surface charge distribution by comparing the data with calculations. With a suitable potential model, which describes the interaction between the helium particle and the crystal surface, and algorithm the surface corrugation is obtained.[3,5]

In the first part of this section particle-surface interaction potential models are described, whereas in the second part approximate methods are presented to calculate the surface corrugation.

2.3.1. Particle-Surface Interaction Potential

When a He-atom reaches the solid surface, an interaction takes place. Since the particle interacts with all atoms of the crystal surface the interaction potential is formed by a total potential $V(\vec{r})$. It depends on the current position of the particle with regard to the surface $\vec{r} = (\vec{R}, z)$, where the coordinates $\vec{R}$ and z are the one presented in chapter 2.2.3. Due to the time dependence of the potential $V(\vec{r}, t)$, it is averaged over the time to describe elastic scattering processes. At a given temperature this is done by fixing the surface atoms at their equilibrium positions.[3]

The interaction potential of a spherical atom like He with the surface atoms consists of two parts. When the particle is close to the surface a repulsion occurs. This is caused by the overlap of the closed-shell electrons of the He-atom and the surface electrons. The Pauli repulsion $V_{rep}(\vec{r})$ describes this part of the potential. At larger distances from the surface the He-particle notices an attractive force, caused by a Van-der-Waals interaction potential $V_{att}(\vec{r})$. Induced polarizations, which occur out of the fluctuating electron density distribution in the particle, are responsible for the attractive forces of the incident He-atom and the surface charge distribution. Summarized, the interaction potential is the sum of a repulsive and an attractive part:

$$V(\vec{r}) = V_{rep}(\vec{r}) + V_{att}(\vec{r}) \tag{2.40}$$

To get the total potential $V(\vec{r})$ the potentials between the He-atom and the surface atoms, i.e. two-body potentials, are summed up. These two-body potentials are assumed to be the one in the gas phase. For ionic crystals this approach is accurate, because of their closed-shell character. In semiconductors and metals the bonding is carried partly by conduction electrons on the surface. In this case this approach should be taken with caution.[3]

The periodic surface structure leads to the assumption that the interaction potential can be expanded in a Fourier Series in terms of the reciprocal lattice vectors $\vec{G}$

$$V(\vec{r}) = V_0(z) + \sum_{\vec{G} \neq 0}^{\infty} V_{\vec{G}}(z) \exp(i\vec{G}\vec{R}) \tag{2.41}$$

The first term $V_0(z)$ is the average potential over the surface.[3,10,24]

Hard-Corrugated-Wall (HCW) Model

The simpliest model for an interaction potential is the Hard-Corrugated-Wall model (HCW), where the attractive part of the potential is neglected. The crystal surface is treated as a hard wall placed at the equilibrium position of the potential with a periodic surface corrugation. The interaction potential is written as follows:

$$V(\vec{R}, z) = \begin{cases} 0 & \text{for } z > \xi(\vec{R}) \\ \infty & \text{for } z \leq \xi(\vec{R}) \end{cases} \tag{2.42}$$

$\vec{R}$ is the lateral position parallel to the surface and z the coordinate normal to the surface. $\xi(\vec{R})$ represents the surface corrugation function, which describes the spatial modulation of the electron density of the surface. It contains the whole information that is obtained from elastic scattering measurements. If the Schrödinger equation is solved for the HCW potential model, it has to fulfill the boundary condition given in 2.42. At the infinite high barrier the wave function has to vanish:[3,5,10,24]

$$\psi(z = \xi(\vec{R}), \vec{R}) = 0 \tag{2.43}$$

9-3 Potential Model

An important two-body potential in the gas phase is the 12-6 Lennard-Jones potential:

$$V(r) = 4\epsilon \left(\left(\frac{\sigma}{r} \right)^{12} - \left(\frac{\sigma}{r} \right)^{6} \right) \tag{2.44}$$

r is the distance between the particles, ϵ is the well depth and σ is the distance where the potential vanishes. The He-atom interacts with every atom on the crystal surface. Thus all two-body interactions have to be summed up to get the total potential. In the continuum limit the sum is replaced by an integral. The integration over the surface leads to the 9-3 potential:

$$V(z) = \left(3^{\frac{3}{2}} \frac{D}{2} \right) \left(\left(\frac{\sigma}{z} \right)^{9} - \left(\frac{\sigma}{z} \right)^{3} \right) \tag{2.45}$$

D is the well depth and σ the distance where the potential equals zero. z is the coordinate normal to the surface. The equilibrium distance for a bound He-atom is at $z = 3^{\frac{1}{6}}\sigma$. One notices that the potential only depends of the z coordinate. The reason for the z dependence is the integration, which is performed over the surface. Two integrations are done over the continuous surface and the third one is done over the depth of the crystal, which leads to the z-dependence.[3,9,10,24]

Lennard-Jones-Devonshire (LJD) Potential Model

Another way to describe the interaction between He-atoms and crystal surfaces is the Lennard-Jones-Devonshire (LJD) potential model:

$$V(\vec{R}, z) = V_0(z) + V_1(z)Q(\vec{R}) \tag{2.46}$$

with

$$V_0(z) = D(\exp(-2\alpha z) - 2\exp(-\alpha z)) \tag{2.47}$$

$$V_1(z) = 2\exp(-2\alpha z)) \tag{2.48}$$

D is the well depth and α is the stiffness parameter. The bare potential is described by $V_0(z)$. To obtain the surface corrugation a corrugation amplitude β is defined. The surface corrugation function $Q(\vec{R})$ depends on the geometry of the crystal surface. Fig. 2.6 shows a contour plot of a Lennard-Jones Devonshire potential of LiF with parameters taken from Wolken.[4,15,24]
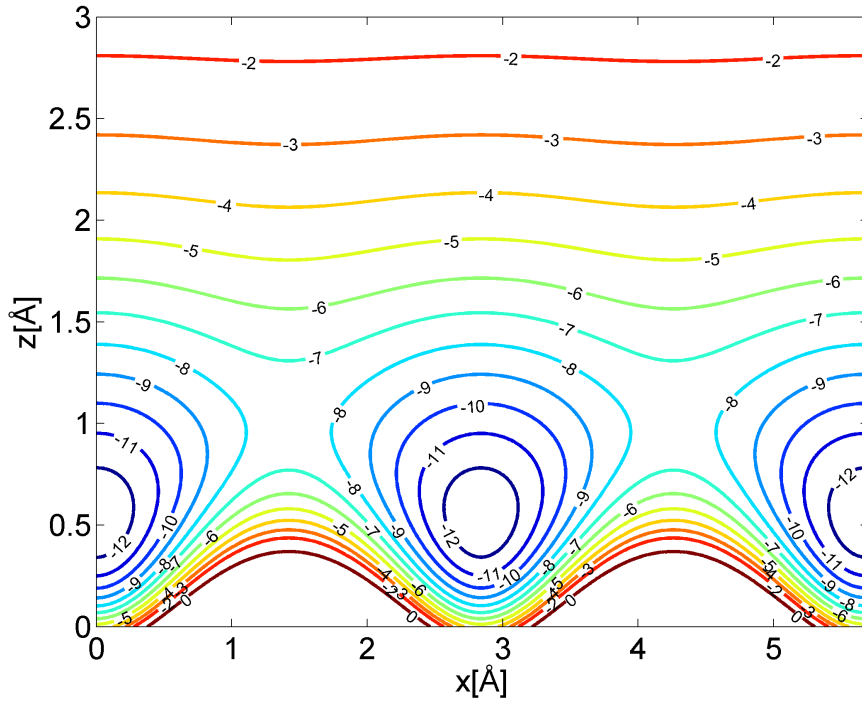
Figure 2.6.: Contour plot of the Lennard-Jones-Devonshire potential for Lithium-fluoride (LiF). The parameters were taken from Wolken to plot the x-z plane.[4]

Morse-Corrugated (MC) Potential Model

An atom-surface potential model originally proposed by Armand and Manson[25] is the Morse corrugated potential model:

$$V(\vec{R}, z) = D\left(\frac{1}{\nu_0}\exp(-2\chi(z - \xi(\vec{R}))) - 2\exp(-\chi z)\right) \tag{2.49}$$

where D is the well depth, χ is the stiffness parameter, $\xi(\vec{R})$ is the surface corrugation function. $\vec{R}$ is a lattice vector on the surface and z the coordinate normal to the surface. ν_0 is the surface averaged potential of the exponential of the shape function:

$$\nu_0 = \frac{1}{S}\int_U \exp(2\chi\xi(\vec{R}))d\vec{R} \tag{2.50}$$

The integration is performed over the unit cell U. The area of the unit cell is described by S. Since the corrugation function is periodic over the surface, the interaction potential can be expanded in a Fourier series as in equ. 2.41. The Fourier coefficients $V_{\vec{G}}(z)$ can be written in terms of the coupling factors $\nu_{\vec{G}}$ as analytical functions:

$$\nu_{\vec{G}} = \frac{1}{S}\int_U \exp(-i\vec{G}\vec{R})\exp(2\chi\xi(\vec{R}))d\vec{R} \tag{2.51}$$

This integral is similar to equ. 2.50, except that the reciprocal lattice vectors $\vec{G}$ are taken into account. The first Fourier coefficient is the bare potential given in equ. 2.47. In the diffraction process higher order coefficients ($\vec{G} \neq 0$) are responsible for the coupling:[24,26]

$$V_{\vec{G}}(z) = \frac{D\nu_{\vec{G}}}{\nu_0}\exp(-2\chi z) \tag{2.52}$$

2.3.2. Calculation of the Surface Corrugation with Approximate Methods

Using quantum mechanics, the scattering of atoms from the surface is described by solving the time independent Schrödinger equation:

$$\left(\frac{h}{2m}\Delta + V(\vec{r})\right)\psi(\vec{r}) = E_i\psi(\vec{r}) \tag{2.53}$$

Since the surface is periodic, the wave function can be expanded in terms of Bloch waves:

$$\psi(\vec{r}) = \psi(\vec{R}, z) = \exp(i\vec{K}_i\vec{R}) + \sum_{\vec{G}}\exp(i\vec{G}\vec{R})\psi_G(z) \tag{2.54}$$

An atom-surface potential model $V(\vec{r})$ is thereby needed to solve the Schrödinger equation as described above.[3]

Elastic scattering intensities are calculated with the Rayleigh assumption using the HCW potential model. The incident and final beams are viewed as plane waves. In the far field of the surface this is true. The wave function $\psi(\vec{R}, z)$ then is:

$$\psi(\vec{R}, z) = \exp(i(\vec{K}_i \vec{R} + k_{iz} z)) + \sum_{\vec{G}} A_{\vec{G}} \exp(i((\vec{K}_i + \vec{G})\vec{R} + k_{\vec{G}z} z)) \qquad (2.55)$$

The first term is the incoming wave and the second term is the sum of all scattered waves, which correspond to a reciprocal lattice vector $\vec{G}$. The scattering amplitudes for each reciprocal lattice vector are described by $A_{\vec{G}}$. $k_{\vec{G}z}$ describes the z-component of the final wavevector. Using the boundary condition 2.43 according to 2.42 leads to:

$$\sum_{\vec{G}} A_{\vec{G}} \exp(i\vec{G}\vec{R} + k_{\vec{G}z}\xi(\vec{R})) = -\exp(ik_{iz}\xi(\vec{R})) \qquad (2.56)$$

If the corrugation function $\xi(\vec{R})$ is known, the scattering amplitudes $A_{\vec{G}}$ can be calculated. This equation has to be fulfilled for every $\vec{R}$ in the unit cell. Different approaches have been invented to solve this equation. They are presented briefly in the following chapters.[3,10]

Eikonal Approximation

When equ. 2.56 is multiplied by $\exp(-i(\vec{G}'\vec{R} + k_{\vec{G}'z}\xi(\vec{R})))$ and integrated over the unit cell, a matrix equation is obtained:

$$M_{\vec{G}\vec{G}'} A_{\vec{G}} = A_{\vec{G}}^{0}{}' \qquad (2.57)$$

with

$$M_{\vec{G}\vec{G}'} = \frac{1}{S} \int_U \exp(i((\vec{G} - \vec{G}')\vec{R} + (k_{Gz} - k_{G'z})\xi(\vec{R}))) \exp(2\chi\xi(\vec{R})) d\vec{R} \qquad (2.58)$$

and

$$A_{\vec{G}}^{0} = -\frac{1}{S} \int_U \exp(-i(\vec{G}\vec{R} + (k_{G'z} - k_{iz})\xi(\vec{R}))) d\vec{R} \qquad (2.59)$$

In the eikonal approximation the non-diagonal elements of $M_{\vec{G}\vec{G}'}$ are neglected for small corrugation heigths. So the assumption is only true for smooth shape functions $\xi(\vec{R})$. $M_{\vec{G}\vec{G}'}$ is the unity-matrix in this approach and thus the scattering amplitudes $A_{\vec{G}}$ become:[3,5,10]

$$A_{\vec{G}} = A_{\vec{G}'}^{0} \qquad (2.60)$$

GR-Method

For larger corrugations another approximate method, the GR-method, to calculate the diffraction peak intensities has to be used. Here equ. 2.56 is multiplied with $exp(ik_{iz}\xi(\vec{R}))$ and the following matrix equation is obtained:

$$\sum_{\vec{G}'} A_{\vec{G}} M_{\vec{G}\vec{R}} = -1 \tag{2.61}$$

with

$$M_{\vec{G}\vec{R}} = \exp(i((k_{Gz} - k_{iz})\xi(\vec{R}) + \vec{G}\vec{R})) \tag{2.62}$$

The matrix equation has to be satisfied by every $\vec{R}$ in the unit cell. A linear equation system of order n is solved to calculate the scattering amplitudes. Therefore a finite set of n vectors $\vec{R}_n$ is chosen, which are associated to the reciprocal lattice vectors $\vec{G}_n$. The linear equation system is solved by matrix inversion to get $A_{\vec{G}}$.[3,5,10]

2.4. Close Coupling (CC) Algorithm

In contrast to the approximate methods described above, the Close Coupling method is a quasi exact method. Due to the fact that the algorithm is very time consuming and the low computer power in early days, this method was not of interest till today. Not only elastic scattering propabilities but also resonances of inelastic scattering processes can be calculated theoretically.

In this section the Close Coupling equations are derived. Afterwards two methods are presented to solve this system of second order differential equations. One approach uses a predictor-corrector Numerov algorithm and the other a Numerov matching method.

2.4.1. Derivation of the Close Coupling Equations

To calculate the diffraction probabilities, the time-independent Schrödinger equation has to be solved numerically (see equ. 2.53). The He-atom with mass m interacts with the crystal surface via the interaction potential $V(\vec{r})$ given in section 2.3.1. The equation has to be solved for positive Eigenvalues E_i, since we have a scattering problem. The energy is equal to the kinetic energy of the incoming particle. It is related to the incident wave vector $\vec{k}_i = (k_{ix}, k_{iy}, k_{iz}) = (\vec{K}_i, k_{iz})$. The components of the wave vector are described in section 2.2.3 and shown in fig. 2.4.[27]

Since the solid surface is periodic, the wave function $\psi(\vec{r})$ can be expanded in a Fourier Series in terms of the reciprocal lattice vectors $\vec{G}$ according to Bloch's theorem:

$$\psi(\vec{r}) = \frac{1}{\sqrt{S}} \sum_{\vec{G}} \phi_{\vec{G}}(z) \exp(i(\vec{K}_i + \vec{G})\vec{R}) \tag{2.63}$$

S is the area of the surface lattice unit cell. Similarly the interaction potential $V(\vec{r})$ can be expanded in a Fourier Series already introduced in equ. 2.41. If this Fourier representation of the potential and the wave function from equ. 2.63 are plugged into the equ. 2.53, the Close Coupling equations are obtained:

$$\left(\frac{d^2}{dz^2} + k_{\vec{G}z}^2 \right) \phi_{\vec{G}}(z) - \sum_{\vec{G}'} V_{\vec{G}-\vec{G}'}(z) \phi_{\vec{G}'}(z) = 0 \tag{2.64}$$

with

$$k_{\vec{G}z}^2 = k_i^2 - (\vec{K}_i + \vec{G})^2 \tag{2.65}$$

The Fourier coefficients $V_{\vec{G}-\vec{G}}(z)$ are responsible for the coupling. They are also known as coupling factors. Depending on the sign of $\kappa_{\vec{G}z}^2$ it corresponds either to open channels ($\kappa_{\vec{G}z}^2 > 0$) or to closed channels ($\kappa_{\vec{G}z}^2 < 0$). Imaginary values of $\kappa_{\vec{G}z}$ belong to decaying waves, whereas real values of $\kappa_{\vec{G}z}$ describe propagating waves. For both cases certain boundary conditions have to be fulfilled:

$$\phi_{\vec{G}}(z) \stackrel{z \to \infty}{\to} \exp(-ik_{iz}z)\delta_{\vec{G},0} + A_{\vec{G}}\exp(ik_{\vec{G}z}z) \text{ for } k_{\vec{G}z}^2 > 0$$
$$\phi_{\vec{G}}(z) \stackrel{z \to \infty}{\to} A_{\vec{G}}\exp(-\kappa_{\vec{G}z}z) \text{ for } k_{\vec{G}z}^2 < 0 \tag{2.66}$$

with

$$\kappa_{\vec{G}z} = (-k_{\vec{G}z}^2)^{\frac{1}{2}} \tag{2.67}$$

In the case of the open channels every propagating wave corresponds to a diffracted beam. The scattering probability $P_{\vec{G}}$ is related to the scattering amplitude $A_{\vec{G}}$ by:

$$P_{\vec{G}} = \frac{k_{\vec{G}z}}{|k_{iz}|}|A_{\vec{G}}|^2 \tag{2.68}$$

If the scattering probabilities are summed up for every open channel, the summation of the intensities has to be equal to one, which is also known as the unitarity condition:[4,10,27]

$$\sum_{\vec{G}, k_{\vec{G}z}^2 > 0} P_{\vec{G}} = 1 \tag{2.69}$$

2.4.2. Predictor-Corrector Numerov Method

The Close Coupling equations are a system of second order differential equations. Since this system cannot be solved for an infinite number of channels, a finite basis set of G vectors is chosen. The basis set size is determined by checking the convergence of the results. Therefore the number of channels N included in the calculation is increased. The number of channels also depends on the energy E_i and it increases for larger energy values. Due to the coupling of the open to the closed channels, some closed channels have to be included in the calculation. These effects are called bound state resonances. The most used interaction potential in close coupling calculations is the Morse corrugated potential model, which is described in section 2.3.1., because the Fourier components $V_{\vec{G}-\vec{G}'}(\vec{r})$ can be calculated analytically in this case.[27]
Usually the numerical integration is done by a predictor-corrector Numerov algorithm originally presented by Baylis.[28] The integration is started at a value z_s, which is far enough in the forbidden region, and thus in the solid. There $\phi_{\vec{G}}(z_s)$ is equal to zero for all N G vectors, which are included in the calculation. With the Numerov algorithm only initial value problems can be solved. Since the differential equation system is of second order, also N independent sets of $\phi'_{\vec{G}}(z)$ at z_s have to be chosen to get N linearly independent solutions. They are propagated to z_e, where the potential is nearly zero. The linear combination of the N solutions has to fulfill the boundary conditions given in equ. 2.66. In this way the scattering amplitudes $A_{\vec{G}}$ and with equ. 2.68 the diffraction probabilities are obtained.[27,28]

2.4.3. Coupling Channels Method

Another approach proposed by Liebsch and Harris[29] is to use a Numerov matching method to solve the Close Coupling equations. The advantage of the method is that numerical instabilities are avoided in contrast to the predictor-corrector Numerov algorithm.
The potential is divided into two parts. The boundary is placed at z_m, which is nearly at the minimum of the interaction potential. In the region $z \leq z_m$ a set of N basis functions $\psi_\alpha(E_i, \vec{K}; \vec{r})$ is constructed, which decay for decreasing values of z. Therefore two initial points z_1 and $z_2 = z_1 + \delta$ are chosen, which are deep in the classical forbidden region. There the potential value $V(\vec{R}, z_1) >> E_i$ is much larger than the energy value E_i. The initial wave function coefficients are the matrices $\psi^{(1)}_{\vec{G}\alpha} = 0$ and $\psi^{(2)}_{\vec{G}\alpha} = \gamma \delta_{\vec{G}\alpha}$. γ is an arbitrary small real number. An iteration outwards with the Numerov algorithm leads to the matrix $\psi = \psi^{(m)}$ at the matching point z_m. The matrix of derivative coefficients is:

$$\Psi' = \frac{1}{6\delta}(\Psi^{(m-2)} - 6\Psi^{(m-1)} + 3\Psi^{(m)} + 2\Psi^{(m+1)}) \tag{2.70}$$

In the region $z \geq z_m$ two kinds of wave functions are constructed. The first one is a basis set of N fuctions $\phi_\alpha(E_i, \vec{K}; \vec{r})$, which either propagate or decay for large z. The second one is a function $\psi_i(E_i, \vec{K}; \vec{r})$, which is propagating towards the surface. They represent diffracted waves (ϕ_α) and the incident wave (ϕ_i) respectively. For the initial points in this region two values z_M and $z_M - \delta$ are chosen. Here the potential is nearly zero. The incident wave ϕ_i and the propagating waves ϕ_α have to be normalized. The normalization is chosen to be:

$$\phi_{\vec{G}i}(E_i, \vec{K}_i; z) = \delta_{\vec{G},0}\kappa_{\vec{G}}^{-\frac{1}{2}}\exp(-i\kappa_{\vec{G}}z)$$
$$\phi_{\vec{G}\alpha}(E_i, \vec{K}_i; z) = \delta_{\vec{G},\alpha}\kappa_{\vec{G}}^{-\frac{1}{2}}\exp(i\kappa_{\vec{G}}z) \tag{2.71}$$

where $\kappa_{\vec{G}}$ is described by:

$$\kappa_{\vec{G}} = \sqrt{k_i^2 - (\vec{K}_i + \vec{G})^2}, \text{ for } k_i^2 \geq (\vec{K}_i + \vec{G})^2$$
$$\kappa_{\vec{G}} = i\sqrt{(\vec{K}_i + \vec{G})^2 - k_i^2}, \text{ for } k_i^2 < (\vec{K}_i + \vec{G})^2 \tag{2.72}$$

The starting coefficients for the evanescent waves are $\phi_{\vec{G}\alpha}^{(M)} = \gamma\delta_{\vec{G}\alpha}$ at z_M and $\phi_{\vec{G}\alpha}^{(M-1)} = \phi_{\vec{G}\alpha}^{(M)}\exp(|\kappa_{\vec{G}}|\delta)$ at z_{M-1}. With the Numerov algorithm an iteration is done inwards till z_m to obtain the matrix $\Phi = \phi_{\vec{G}\alpha}^{(m)}$ and the vector $\Phi_i = \phi_{\vec{G}i}^{(m)}$. The derivative coefficients at z_m are given by:

$$\Phi' = -\frac{1}{6\delta}(\Phi^{(m+2)} - 6\Phi^{(m+1)} + 3\Phi^{(m)} + 2\Phi^{(m-1)}) \tag{2.73}$$

The same is valid for the vector Φ_i'.[29]

In the two regions the following conditions are satisfied by the basis functions:

$$\Psi^+\Psi' - \Psi'^+\Psi = 0$$
$$\Phi^+\Phi' - \Phi'^+\Phi = 2i(c_\alpha\delta_{\alpha\beta})$$
$$\Phi^+\Phi_i' - \Phi'^+\Phi_i = 0$$
$$\Phi_i^+\Phi_i' - \Phi_i'^+\Phi_i = -2i \tag{2.74}$$

c_α is equal to one for propagating waves and zero otherwise. These equations are very useful to check the accuracy of the numerical integration.[29]

The solutions at the matching point are also an independent set of basis functions, since the integrations in both regions were started with linearly independent column vectors. The scattering state can be expanded as follows:

$$\psi(E_i, \vec{K}_i; \vec{r}) = \sum_{\alpha=1}^{N} \psi_\alpha(E_i, \vec{K}_i; \vec{r}) T_\alpha(E_i, \vec{K}_i) \ z \leq z_m$$

$$\psi(E_i, \vec{K}_i; \vec{r}) = \phi(E_i, \vec{K}_i; \vec{r}) - \sum_{\alpha=1}^{N} \phi_\alpha(E_i, \vec{K}_i; \vec{r}) R_\alpha(E_i, \vec{K}_i) \ z \leq z_m \qquad (2.75)$$

By matching ψ and its normal derivative $\psi' = \partial\psi/\partial z$ along the plane at z_m, the reflection and transmission coefficients, R_α and T_α, can be determined. A set of 2N equations are created as follows:

$$\sum_{\alpha=1}^{N} \psi_{\vec{G}\alpha} T_\alpha = \phi_{\vec{G}i} - \sum_{\alpha=1}^{N} \phi_{\vec{G}\alpha} R_\alpha$$

$$\sum_{\alpha=1}^{N} \psi'_{\vec{G}\alpha} T_\alpha = \phi'_{\vec{G}i} - \sum_{\alpha=1}^{N} \phi'_{\vec{G}\alpha} R_\alpha \qquad (2.76)$$

In matrix notation this leads to:

$$\Psi T = \Phi_i - \Phi R, \ \Psi' T = \Phi'_i - \Phi' R \qquad (2.77)$$

The solution for the reflection coefficient is:

$$R = (\Phi' - \Psi'\Psi^{-1}\Phi)^{-1}(\Phi'_i - \Psi'\Psi^{-1}\Phi_i) \qquad (2.78)$$

The gth diffracted beam intensities are then given by:

$$I_{\vec{G}} = |R_{\vec{G}}|^2 \qquad (2.79)$$

with

$$\sum_{\vec{G}} I_{\vec{G}} = 1 \qquad (2.80)$$

The sum again is done over non-evanescent beams. In principle an exact solution of the elastic scattering problem is found with this algorithm.[29]

2.5. Numerical Computation of the Temperature Distribution in Matter

In order to calculate boundary value and/or initial value problems, the finite-element-method (FEM) is a powerful numerical method widely used in engineering fields such as thermodynamics and mechanics. In this case we are dealing with heat conduction problems and thus the heat equation is of interest. First of all

the variational formulation of the partial differential equation has to be found. The heat equation also has to satisfy certain boundary conditions. If the problem is dynamic, additionally an initial value has to be defined. To solve the 2D heat equation numerically the FEM algorithm is briefly described in this section. The new temperature distribution is then calculated by solving a simple linear equation system. Finally a way how to treat nonlinear dynamic problems is shown.

2.5.1. Modeling of the Heat Conduction Problem

At first the partial differential equation that describes the problem has to be formulated. In this case the two-dimensional heat conduction equation is written as:

$$\rho c_p \frac{\partial T}{\partial t} = \lambda \left(\frac{\partial^2 T}{\partial x^2} + \frac{\partial^2 T}{\partial y^2} \right) \tag{2.81}$$

λ is the heat conductivity, c_p the specific heat capacity and ρ is the density of the material. It is assumed that these parameters are isotropic and time independent. The aim is to find the function $T = T(x, y, t)$ that solves the heat equation. This function should be determined in a basic domain $(x, y) \in \Omega$ and at a specific initial time $t \geq t_0$. The problem is also defined by some additional conditions that the solution function $T(x, y, t)$ has to fulfill. Since the differential equation is of first order in time, an initial value condition has to be satisfied:

$$T(x, y, t_0) = T_0(x, y) \text{ for } (x, y) \in \Omega \tag{2.82}$$

Furthermore, the behaviour of the function on the boundary R of the basic domain Ω has to be determined. If function values of the solution are given on the boundary, a Dirichlet boundary condition is given:

$$T(x, y, t) = T_R(x, y, t) \text{ for } (x, y) \in R \tag{2.83}$$

For the Cauchy boundary condition, values of the derivative of T are given in the direction of the vector normal to the boundary $n = (n_x, n_y)^T$:

$$\lambda \left(\frac{\partial T}{\partial x} n_x + \frac{\partial T}{\partial y} n_y \right) + a_4 T = a_5 \text{ for } (x, y) \in R \tag{2.84}$$

a_4 and a_5 are functions of x, y and t defined at the boundary. If $a_4 = 0$ and $a_5 \neq 0$ an inhomogenous Neumann condition is given. For the homogenous Neumann condition both coefficients vanish.[30]

2.5.2. Numerical Solution with the FEM

The starting point of the FEM algorithm is the application of a variational principle on the heat conduction problem. The function $T(x, y, t)$ which makes the integral expression

$$I(f) := \int_\Omega dx dy \left(\frac{\lambda}{2}(T_x^2 + T_y^2) + \rho c_p T_t T \right) + \int_R ds \left(\frac{a_4}{2}T^2 - a_5 T \right) \qquad (2.85)$$

stationary with respect to the initial value and boundary value conditions solves the boundary value problem.[30]

To evaluate the surface integral, the basic domain is subdivided into a finite number n of triangles, which is also known as triangulation. This yields to the following expression:

$$I(f) := \sum_{m=1}^{n} I_m + R_f \qquad (2.86)$$

with

$$I_m := \int_{D_m} dx dy \left(\frac{\lambda}{2}(T_x^2 + T_y^2) + \rho c_p T_t T \right) \qquad (2.87)$$

and

$$R_f := \int_R ds \left(\frac{a_4}{2}T^2 - a_5 T \right) \qquad (2.88)$$

where D_m is the mth triangle on the basic domain Ω. For the total integral expression I(f), terms over all n triangles and terms over all boundary lines have to be summed up. If the extremal principle is applied every term has to be differentiated by the points of the triangles or the boundaries. The results of the calculations are then set equal to zero. Out of the linear equation system the solution $T(x, y, t)$ is computed:

$$A(T)T + BT_t = f(T) \qquad (2.89)$$

where A and B are symmetric matrices and f is an inhomogenic vector. Notice that A and f are functions of the temperature and thus nonlinear. For a detailed derivation of equ. 2.89 I refer to the lecture notes about the FEM by Sormann.[30]

2.5.3. Computation of the New Temperature Distribution

To treat dynamic problems numerically, a simple difference method can be used. Therefore the time t is subdivided into finite timesteps Δt. It is assumed that the

temperature $T(t)$ at the time t is known and the temperature $T(t + \Delta t)$ at time $t + \Delta t$ has to be computed. The time derivative is approximated by the differential quotient:

$$T_t(t + \Delta t) \approx \frac{T(t + \Delta t) - T(t)}{\Delta t} \tag{2.90}$$

For the temperature vector T(t) the average value over the time interval $[t, t + \Delta t]$ is used. Under these considerations the following difference equation is obtained for the timestep $t \rightarrow t + \Delta t$:

$$B\frac{T(t + \Delta t) - T(t)}{\Delta t} + A(T_1)T_1 - f(T_1) = B\frac{T(t + \Delta t) - T(t)}{\Delta t} + C(T_1) = 0 \tag{2.91}$$

with

$$T_1 = \frac{T(t + \Delta t) + T(t)}{2} \tag{2.92}$$

One notices that this is a nonlinear equation system. The problem is avoided if the Matrix $C(T_1)$ is linearized at the time $\frac{(t+\Delta t)+t}{2}$ in the following way:[31]

$$C(T_1) = C(T_0) + J(T_0)(T_1 - T_0) \tag{2.93}$$

Here T_0 is the initial temperature and $J(T_0)$ is the Jacobi matrix. Plugging this into equ. 2.91 and transforming it yields an approximate expression for the new temperature:

$$T(t + \Delta t) = T_0 - \frac{C(T_0)}{D(T_0)} \tag{2.94}$$

with

$$D(T_0) = \frac{B}{\Delta t} + \frac{J(T_0)}{2} \tag{2.95}$$

Further details about heat conduction problems are found in the book of Steinke.[30,32]

3. Improvements of the Apparatus

In this section the enhancements of the helium atom scattering (HAS) machine are shown. The apparatus itself was bought in 2007 from the Free University of Berlin by the Technical University of Graz. Until 2009 the machine was remounted. Also first calibration measurements were done by Nikolaus Balak for his diploma thesis.[8]

Three main parts form the HAS apparatus (see fig. 3.1). In the first one, which is the source arm, the helium beam is generated. In the second one, the main chamber, the sample is mounted and several measurement devices (A quadrupol mass spectrometer (QMS), an auger electron spectroscopy device (AES) and a low energy electron diffraction device (LEED)) are placed around it. Finally, the third one is the detector arm, where the helium signal is detected using a cross-beam ion source and a QMS. Four differential pumping stages are used to distinguish between He-atoms that are scattered from the surface and background particles. During a measurement the collimated helium beam hits the sample at an incident angle Θ_i normal to the surface. After the helium atoms scatter from the surface, they reach the detector arm at a final angle Θ_f. When the sample is rotated, both angles are changed simultaneously. An important fact about the machine is that the angle between the source arm and the detector arm $\Theta_{SD} = \Theta_i + \Theta_f = (91.5 \pm 0.6)°$ remains constant.[3,5]

Several improvements were done during the research for this Master thesis. One was an implementation of a limiting circuit for the button heater, so that the sample does not get too hot and consequently causes damage through the heating process. Another one was the mounting of a new venting valve, which vents the main chamber with a gas other than the gas mixture air. The aim is to prevent the main chamber from water (H_2O) vapour. It is expected that less water is in the main chamber if it is vented with a different gas than air. Therefore QMS measurements were done to compare the venting with air to the venting with a different gas. Furthermore temperature measurements of a cold head were done with small and large loads, to obtain the end temperature. Two measurement circuits for a Pt100 element have been studied. Also a finite elements method (FEM) analysis was done to simulate the cooling process of the copper string,

which is placed between the cold head and the sample.
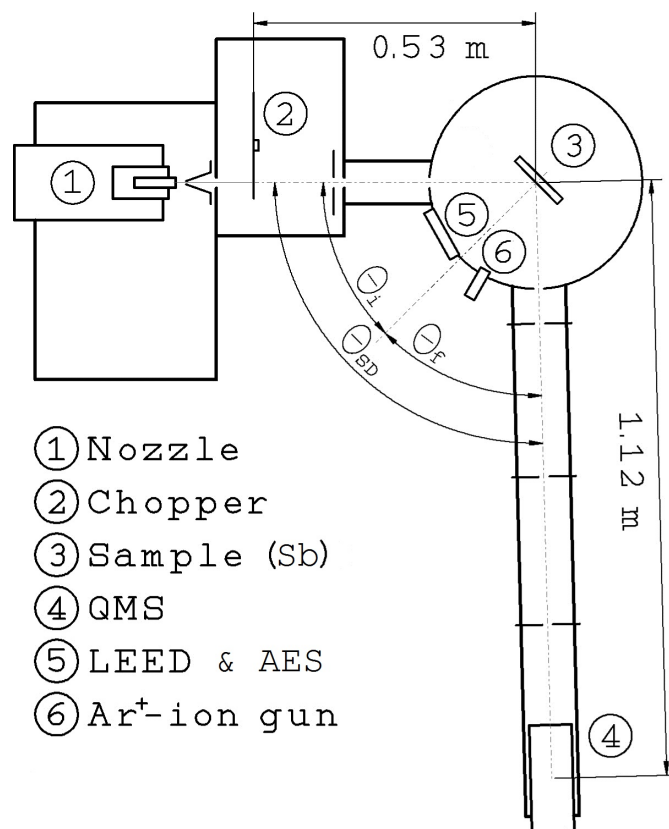
Figure 3.1.: Schematic drawing of the HAS apparatus. Notice that the angle between the source arm and the detector arm remains constant.[5]

3.1. Limiting Circuit for the Button Heater

The heating of the sample is important in order to reach the purity of the sample. There are two methods to heat the sample. The first one uses a Thermocoax, which is wound around the liquid nitrogen reservoir in the main chamber. The second one uses a button heater, which is placed directly behind the sample and thus local heating is achieved. To control the Thermocoax current, a simple laboratory transformer was used. The temperature of the button heater on the contrary is controlled by a temperature control unit (EUROTHERM 3208). A power supply (EA-PS 3016-10B) provides the current for the buttonheater.

A problem arises, when the button heater gets a temporary high voltage peak due to the PID-controller. In that case the sample gets very hot for a short time and can cause damage.

To prevent this, a limiting circuit for the buttonheater was implemented within the temperature control unit and the power supply.

3.1.1. Dimensioning of the Circuit

The limiting circuit is built between the temperature control unit and the power supply. The input voltage U_{in} of the power supply ranges from (0-10) V and the output voltage U_{out} from (0-16) V. This leads to a multiplication factor f of about:

$$f = \frac{U_{in}}{U_{out}} = \frac{10}{16} \approx 0.6 \tag{3.1}$$

The pin assignments, which where used for the circuit and are shown in the graphics, are listed and briefly described in table 3.1 below:

Table 3.1.: Pin assignments for the limiting circuit:

| pin | ... | pin labels used in the drawings |
| description | ... | brief description of the different pins |

pin	description
HD/HE/HF	RS 232 connection
V+/V-	thermo couple connection
3A/3B	circuit connection
L/V	supply voltage connection
VSEL	nominal value voltage (0-10) V
CSEL	nominal value current (0-10) V
VREF	reference voltage (10 V, Imax: 5 mA)
DGND	digital ground (ground for operating and reporting signals)
SEL-Enable	toggle Local/Extern (U$_{max}$: 20 V, I$_{max}$: -25 mA)

In fig. 3.2 the circuit to reduce the output voltage is depicted. The temperature control unit delivers a maximum current of $I_{max} = 20$ mA. The input voltage should not get higher than 3 V. We then get a resistance R_0 of about:

$$R_0 = \frac{U_{in}}{I_{max}} \approx 150 \ \Omega \tag{3.2}$$

This is realised with two varying ohmic resistors of 100 Ω.

The circuit to reduce the input voltage is shown in fig. 3.3. It is dimensioned so that the input voltage is reduced from $U_0 = 10$ V to $U_1 = 2$ V at an incoming current of $I = 1$ mA. This leads to a resistance R_1 of:

$$R_1 = \frac{U_1}{I} = 2 \ \text{k}\Omega \tag{3.3}$$

This is realised with an varying ohmic resistor of 10 kΩ.
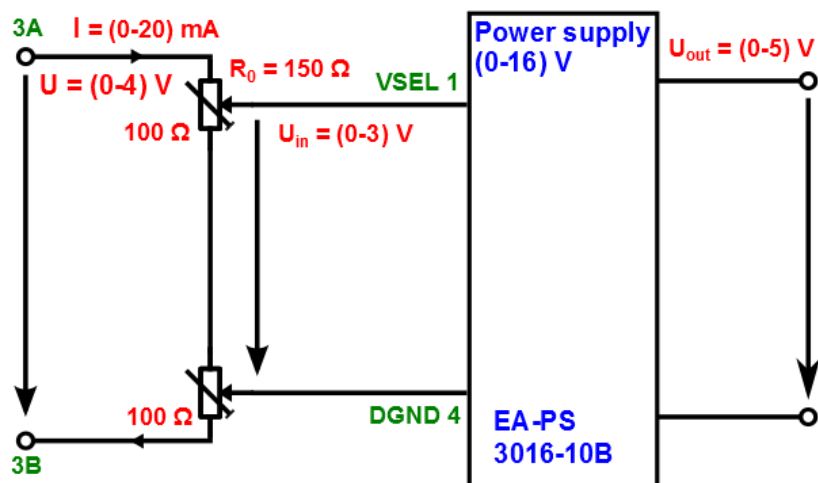
Figure 3.2.: Two varying ohmic resistors are used to reduce the output voltage. With a resistance of about 150 Ω an outpult voltage of 5 V is achieved.
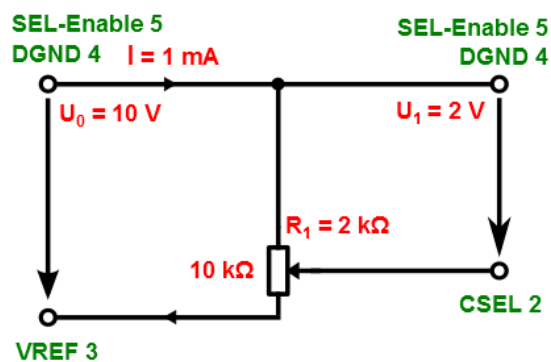
Figure 3.3.: A varying ohmic resistor is used to reduce the input voltage. With a resistance of 2 kΩ an input voltage of 2 V is achieved.

The whole limiting circuit is depicted in fig. 3.4. The advantage of the varying ohmic resistors is that the limited output voltage can be adjusted to other samples in the future.
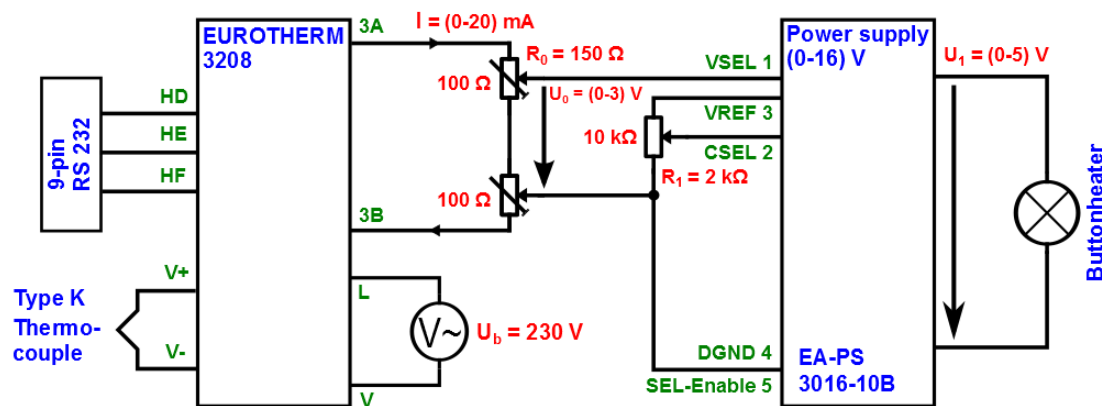
Figure 3.4.: The whole limiting circuit is shown. The varying ohmic resistors can be attached to other samples in the future.

3.2. Venting Valve Measurements of the Main Chamber

In the ultra high vacuum (UHV) region the sample surface stays clean for a longer time, because the lower the pressure in the main chamber is, the longer the coverage time of the crystal surface gets. This way it is possible to perform HAS experiments in the time range of days before the sample surface has to be cleaned again. When a new sample is mounted, the main chamber is vented with air. The UHV then is reached again by a pumpout process and a bakeout process of the main chamber. Two turbo molecular pumps (TMP) form the main part of the pumping. The heating process is done with several heating wires.

The biggest problem is that the above described process takes rather long, because of the large amount of water that comes from the humidity right after the main chamber is vented with air. If a different venting gas is used, it is expected that the amount of water is much lower in the beginning and thus the pumpout process is faster.

Therefore a new venting valve (Pfeiffer TVF 005) was mounted, which is connected to the venting gas and the electrical control device for the TMP. The main chamber can either be vented automatically, when the rotary frequency of the TMP undergoes a certain frequency, or manually. The usual venting time is about ten minutes.

In this section the bakeout process is investigated. Afterwards, three venting gases (air, argon and nitrogen) are compared with each other. The analysis is done in both cases by QMS measurements of the residual gas in the main chamber.

3.2.1. The Bakeout Process

As mentioned above, the heating process of the main chamber is an important part to obtain UHV. To investigate this process in detail, QMS measurements were done before, during and after the bakeout process.

When a molecule reaches the QMS it is ionized and accelerated to the detector. With a certain probability (fragmentation probability) parts of the molecule are splitted off. Water (H_2O) for example has the fragments HO, O, H_2 and H. Due to the bombardement of the molecule with electrons, there is also a probability (ionization probability) that the molecule is found in a higher ionization state. These two competing processes make it difficult to calculate partial pressures out of a MS. QMS signal ratios of molecules with its fragments were calculated (see fig. 3.5). A certain mass number therefore is usually represented by more than one molecule.[6]
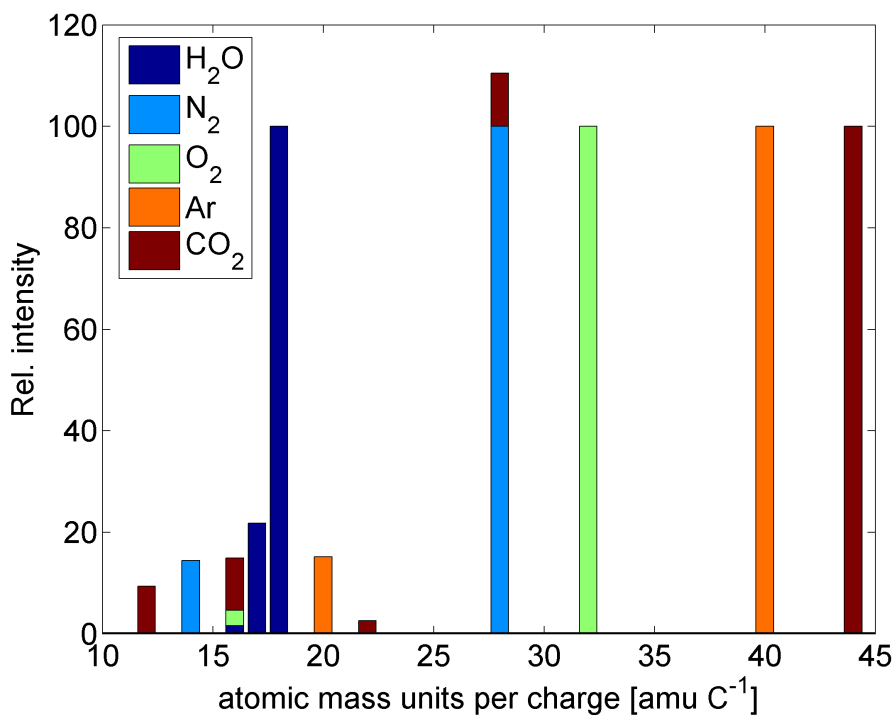
Figure 3.5.: Fragments and ionization states of different molecules. The data was taken from the NIST homepage.[6]

In the following tab. 3.2 the fragmentation and ionization of different molecules are listed:

Table 3.2.: Fragments of important molecules:

<div align="center">

name   ...   name of the molecule
formula   ...   formulas of the fragments
amu/q [amu/C]   ...   atomic mass units per charge in amu/C
rel. intensity   ...   relative intensity of the fragments.

</div>

name	formula	amu/q [amu/C]	rel. intensity
water (H_2O)	H_2O^+:HO^+:O^+	18:17:16	100:21.8:1.6
nitrogen (N_2)	N_2^+:N^+	28:14	100:14.4
oxygen (O_2)	O_2^+:O^+	32:16	100:3
argon (Ar)	Ar^+:Ar^{2+}	40:20	100:15.2
carbondioxide (CO_2)	CO_2^+:CO^+:CO_2^{2+} : :O^+:C^+	44:28:22: :16:12	100:10.5:2.6: :10.3:9.4

Before the Bakeout

In fig. 3.6 a mass spectrum (MS) before the bakeout process is shown.
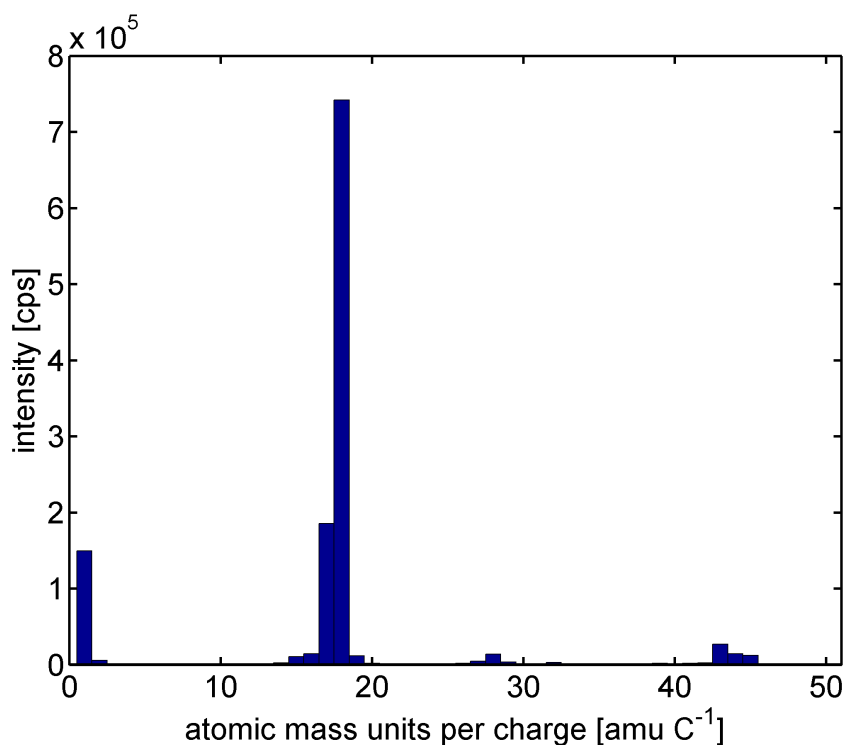
Figure 3.6.: Mass spectrum before the bakeout-process. The QMS signal of water at 18 is very high, which limits the obtainable pressure in the main chamber.

Table 3.3 lists the most important peaks of the MS and assigns possible molecular ions to them:

Table 3.3.: Important peaks before the bakeout process:

amu/q [amu/C]	...	atomic mass units per charge in amu/C
intensity [cps]	...	QMS signal in cps
ions	...	possible ions for the mass number

amu/q [amu/C]	intensity [cps]	ions
1	149000	H^+, H_2^{2+}
2	5700	H_2^+
14	2600	N^+
16	14300	O^+
17	186000	HO^+
18	740000	H_2O^+
28	14000	CO^+, N_2^+
32	3200	O_2^+
44	14500	CO_2^+

The MS in fig. 3.6 was recorded 17 h after the main chamber was vented and closed. The pressure of the main chamber was $2.4 \cdot 10^{-7}$ mbar. The temperature of the main chamber was 20 °C and of the sample 30 °C. The ratio from above is fulfilled approximatively for water. Thus, we can safely say that the QMS signal at 18 comes from water. As expected, the water signal is very high before the bakeout. This means that the contribution to the total pressure in the main chamber mainly comes from the water.

During the Bakeout
During the bakeout process the time dependent water signal is of interest (see fig. 3.7). The MS was recorded 24 h after the main chamber was vented. The pressure range of the main chamber was $(1.0 - 1.8) \cdot 10^{-6}$ mbar. The temperature range of the main chamber was (32-45) °C and of the sample (185-210) °C. The QMS signal of water increases, which means that the water is evaporating off the walls from the main chamber. Thus also the total pressure increases during the bakeout until it reaches a maximum.
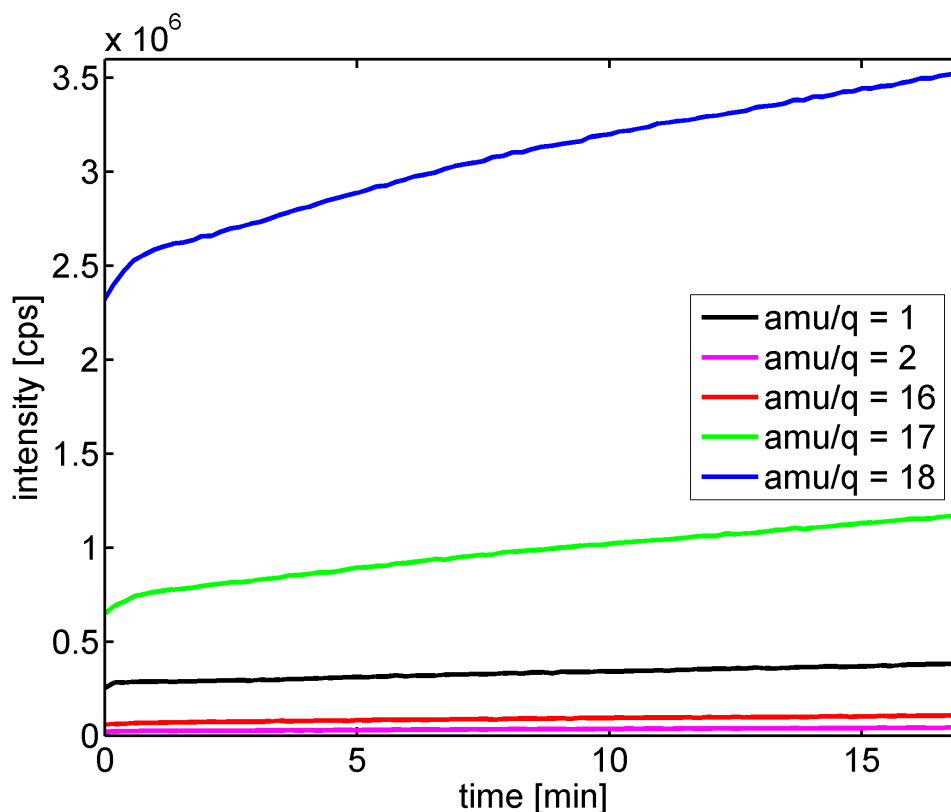
Figure 3.7.: Time dependent QMS signals of water and its fragments during the bakeout. The higher the signals the higher the total pressure in the main chamber.

After the Bakeout

The MS in fig. 3.8 was recorded 66 h after the main chamber was vented and closed. The pressure range of the main chamber was $2.5 \cdot 10^{-8} - 8.3 \cdot 10^{-10}$ mbar. The temperature range of the main chamber was (107-60) °C. The sample temperature was 140 °C. After the bakeout the water signal decreases exponentially, because after heating up the main chamber the evaporated water is pumped by the TMPs. In that way it is possible to lower the total pressure of the main chamber by about two magnitudes.

Residual Gas Analysis

When the end pressure is achieved, a residual gas is still in the main chamber (see fig. 3.9). The MS was recorded 89 h after the main chamber was vented and closed. The pressure of the main chamber was $4.0 \cdot 10^{-11}$ mbar. The temperature of the main chamber was 20 °C and of the sample 30 °C. One notices that the water signal is very low now in comparison to the MS before the bakeout.
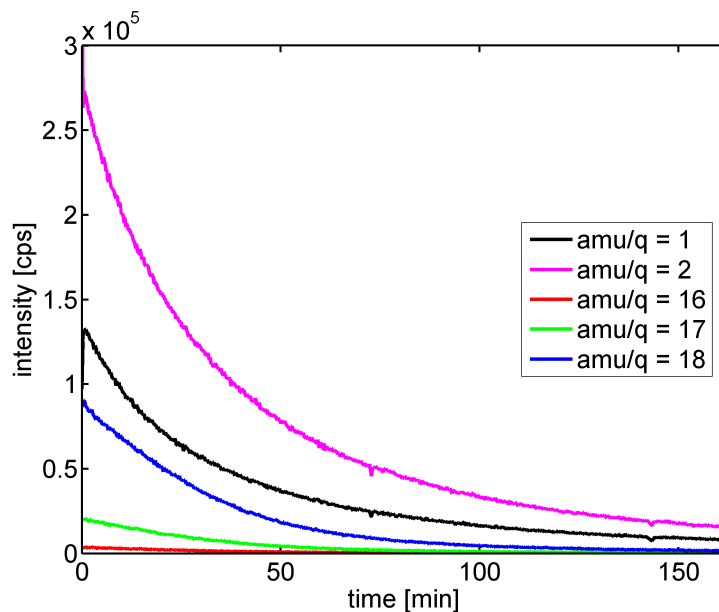
Figure 3.8.: Time dependent QMS signal of water and its fragments after the bakeout. The signals decrease exponentially, which means a much lower total pressure in the end than before the bakeout.
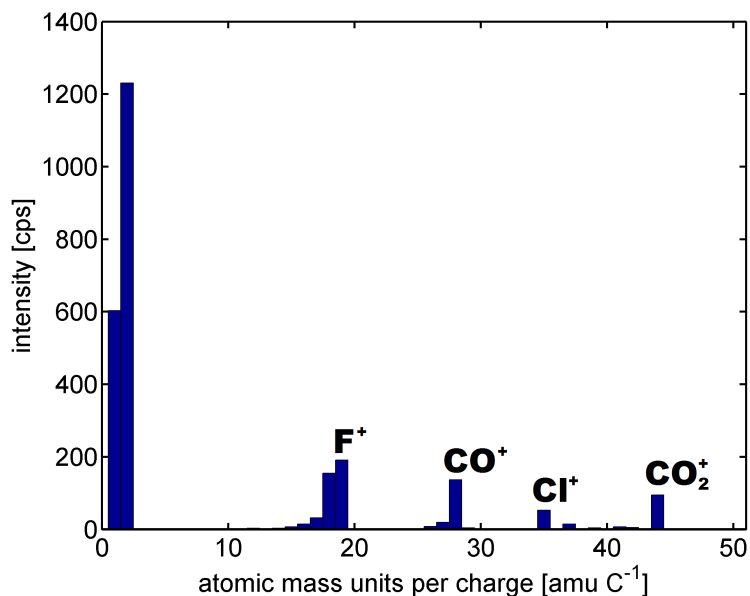
Figure 3.9.: Mass spectrum of the residual gas. The fluorine (F) and chlorine (Cl) result out of cleaning the copper parts with an CFC. Carbon monoxide (CO) and Carbon dioxide (CO_2) are created when the tungsten filaments are heated up and carbon binds with the surrounding oxygen.

The following table 3.4 lists the most important peaks of the MS in increasing order and assigns possible molecule structures to them:

Table 3.4.: Important peaks after the bakeout process:

amu/q [amu/C]   ...   atomic mass units per charge in amu/C
intensity [cps]   ...   QMS signal in cps
ions   ...   possible ions for the mass number

amu/q [amu/C]	intensity [cps]	ions
1	600	H^+,H_2^{2+}
2	1230	H_2^+
17	32	HO^+
18	160	H_2O^+
19	190	F^+
28	140	CO^+,N_2^+
35	53	Cl^+
44	95	CO_2^+

The signals at mass numbers 19 and 35 for fluorine (F) and chlorine (Cl) respectively are coming from copper parts cleaned with a Chlorofluorocarbon (CFC). The signals at mass numbers 28 and 44 are typical for carbon monoxide (CO) and carbon dioxide (CO_2), respectively. In certain devices, tungsten filaments are used to generate free electrons out of thermal emission. During the bakeout the carbon, which adsorbated on the filaments, binds with the oxygen to CO and CO_2 and evaporates in the chamber.

A leakage in the main chamber is identified by the QMS signals of molecular nitrogen and oxygen (28 and 32). The ratio of the signals then is about 4 : 1. Also the QMS signals at 14 and 16 for nitrogen and oxygen respectively have to be observed. These signals are characteristic for air, which is the main part of a leakage. When the crystal surface is sputtered with Ar^+-ions, the signals at 20 and 40 increase. Since the software records the ratio between the mass number and the charge, one gets a signal at 40 for the Ar^+-ions and a signal at 20 for the Ar^{2+}-ions. The ratio of the heights is about 1 : 7.[6,33]

3.2.2. Venting Gas Comparison

After the main chamber is vented, it is pumped out first by pre-vacuum pumps until a pressure of $2.5 \cdot 10^0$ mbar is reached. Then the TMPs are turned on and a longtime MS is recorded with the QMS. When a pressure of $5 \cdot 10^{-8}$ mbar is reached, another longtime MS is recorded. This procedure was done for air, nitrogen and argon respectively.

In fig. 3.10 the time dependent water signal is shown. As expected, the signal for venting with air is much higher than for venting with argon or nitrogen. One notices the great peak at the beginning in the case of argon. At that time the pressure gauge was turned on while the MS was recording. Out of the distortion of the argon measurement only the nitrogen measurement can be compared to the air measurement.
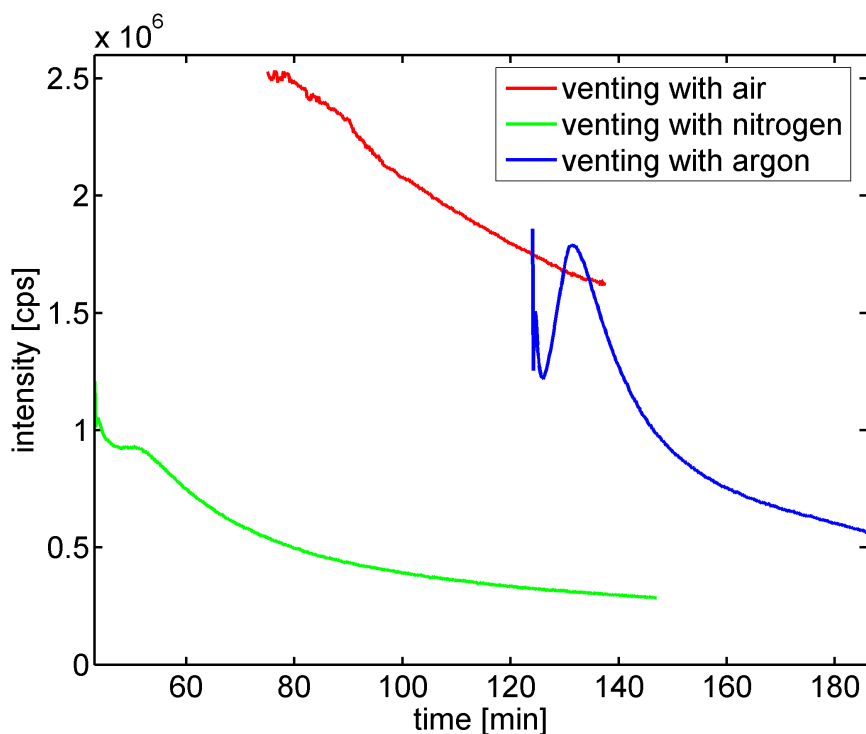
Figure 3.10.: Time dependent QMS signal of water. One notices that the signal for venting with air is much higher than for venting with argon and nitrogen. Since the signal is distorted for the argon measurement, as one can see from the high peak at the beginning, only the nitrogen measurement can be compared to the air measurement.

At the same time of 137 min the total pressure for the nitrogen measurement is much lower than for the air measurement (see fig. 3.11). This means that the pump out process is actually faster, if the main chamber is vented with nitrogen.
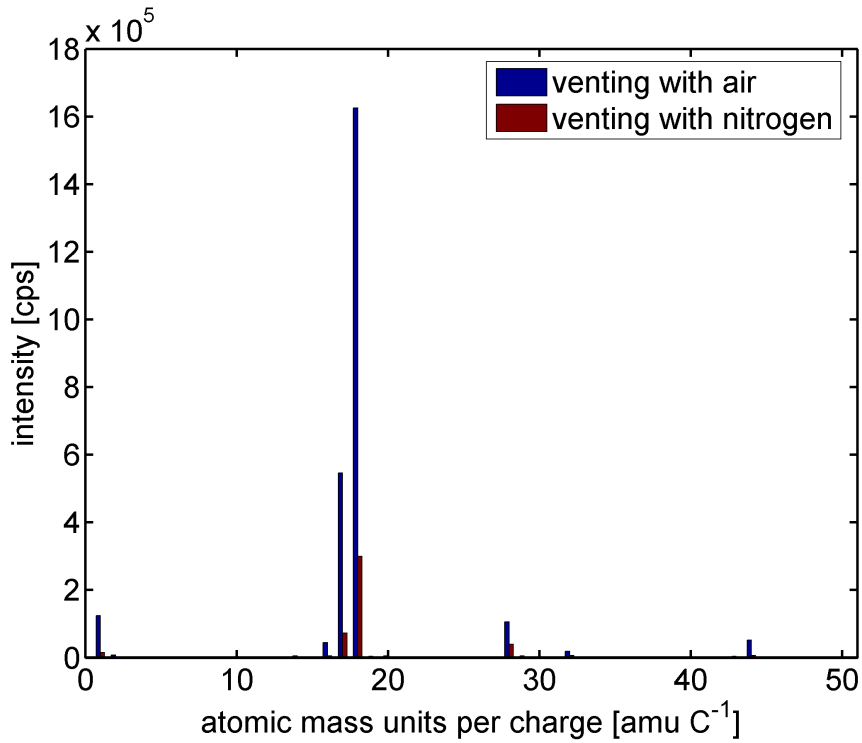
Figure 3.11.: Mass spectrum at the time of 137 min. The signals for venting with nitrogen are much lower than for venting with air.

Table 3.5.: Comparison of the QMS signals after 137 min:

amu/q [amu/C]	...	atomic mass units per charge in amu/C
intensity (air) [cps]	...	QMS signal in cps for air
intensity (N_2) [cps]	...	QMS signal in cps for nitrogen
ions	...	possible ions for the mass number

amu/q [amu/C]	intensity (air) [cps]	intensity (N_2) [cps]	ions
1	125000	15700	H^+, H_2^{2+}
2	7400	1200	H_2^+
16	45000	6000	O^+
17	546000	72600	HO^+
18	1625000	300000	H_2O^+
28	106000	39300	CO^+, N_2^+
32	18600	7300	O_2^+
44	52300	7200	CO_2^+

Table 3.5 lists the most important peaks of the MS for nitrogen and air respectively in increasing order and assigns possible molecule structures to them.

At a pressure of about $5 \cdot 10^{-8}$ mbar the gas in the main chamber consists approximately of the same components for air and nitrogen respectively (see fig. 3.12). The only difference is that this pressure is reached faster with nitrogen than with air.
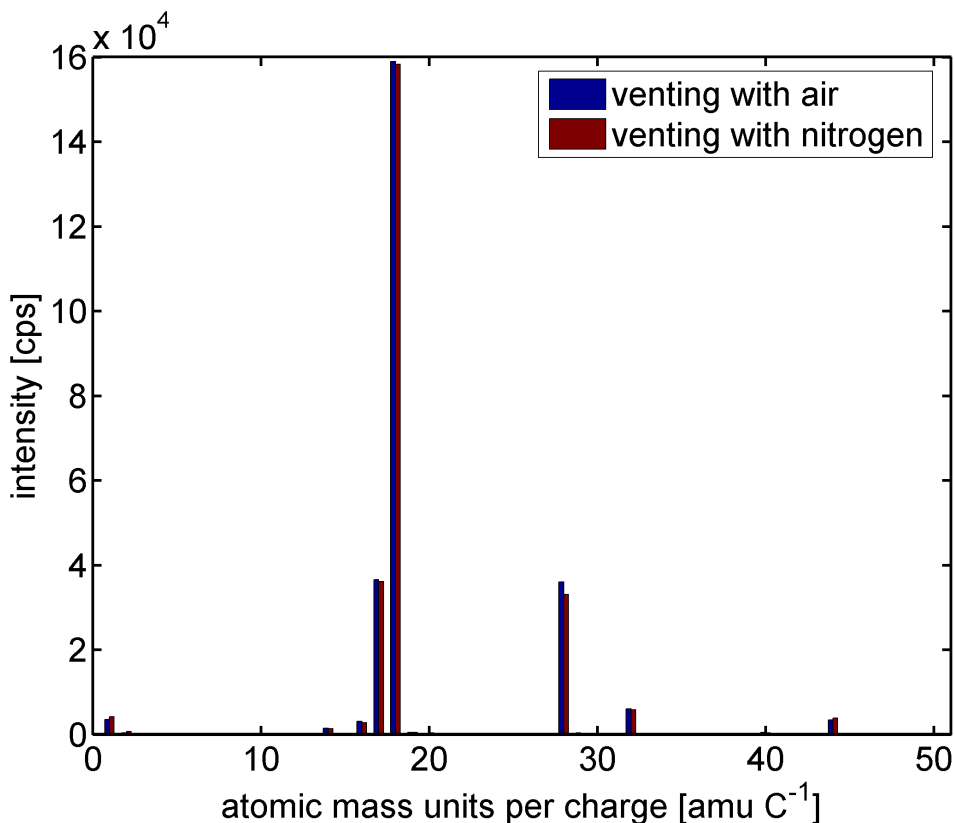
Figure 3.12.: Mass spectrum at a total pressure of about $5 \cdot 10^{-8}$ mbar. The residual gas for air and nitrogen consists of the same components.

3.3. Temperature Measurements of the Cold Head RGD1245

Until now the sample in the chamber has been cooled down with liquid nitrogen to make measurements in the temperature range of 100 K possible. Therefore a big dewar vessel, which contains about 100 l, always has to be filled and subsequently was connected to the liquid nitrogen reservoir of the main chamber.

To avoid this time consuming part of fetching the liquid nitrogen, the sample in

the future will be cooled down with a cold head. As another advantage, deeper temperatures can be achieved.

As a testing system a small vacuum chamber was built for temperature measurements of the cold head (see fig. 3.13). Two temperature measurement circuits were studied for a Pt100 element. A Type-K thermocouple was used as a reference. Then the time dependence of the temperature was investigated for a small load, which was made of a copper disk with a diameter of 54 mm and a thickness of 13 mm and has a mass of 265 g. Afterwards, the sample holder in the main chamber was simulated with aluminum parts at the end of a copper string of a certain length (large load). The cooling process of this copper string was theoretically analysed by the finite-elements-method (FEM).
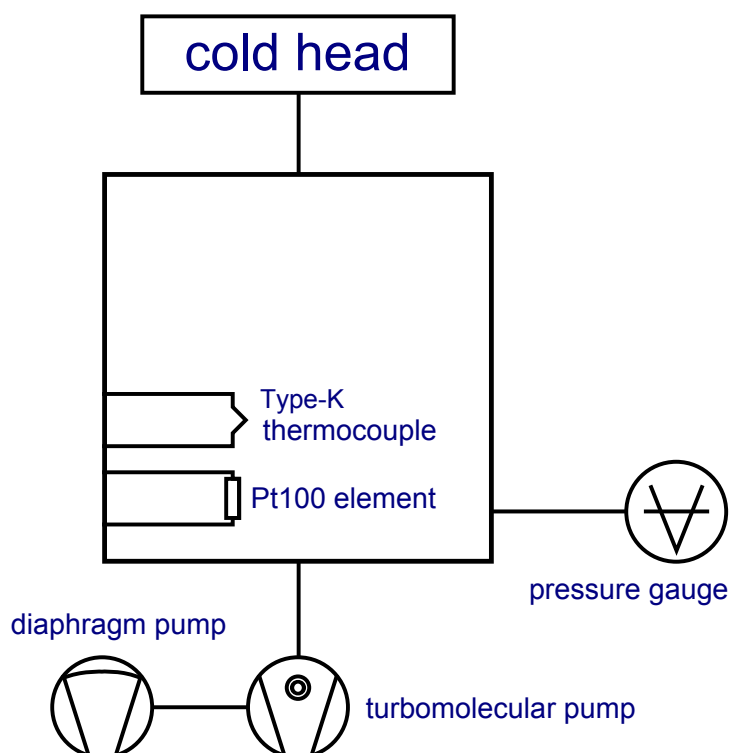
Figure 3.13.: Schematic drawing of the testing system. It was realised with a small vacuum chamber.

3.3.1. The Pt100 Element

A platinum-wire that changes its resistance drastically with the temperature and has its nominal value of $R_0 = 100 \ \Omega$ at $T = 0 \ \text{°C}$, is called a Pt100 element. The characteristic temperature dependence of the resistance is described by the following polynomials:[34]

$$R_2 = R_0(1 + AT + BT^2 + C(T - 100)T^3) \qquad (T < 0 \;°\text{C}) \qquad (3.4)$$

$$R_2 = R_0(1 + AT + BT^2) \qquad (T > 0 \;°\text{C}) \qquad (3.5)$$

The coefficients are $A = 3.9083 \cdot 10^{-3} \;°\text{C}^{-1}$, $B = -5.775 \cdot 10^{-7} \;°\text{C}^{-2}$ and $C = -4.183 \cdot 10^{-12} \;°\text{C}^{-3}$. The characteristic curve is depicted in fig. 3.14. The resistance falls with decreasing temperature.
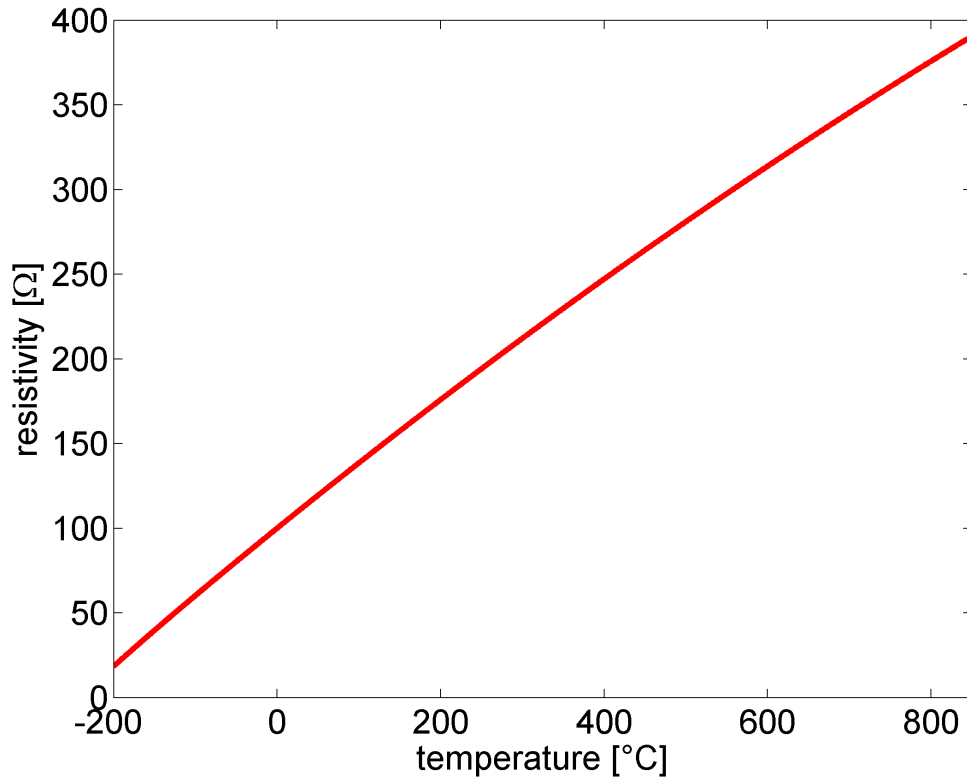
Figure 3.14.: Temperature characteristic of a Pt100 element. The lower the temperature, the lower the resistance gets.

3.3.2. First Temperature Measurement Circuit

A two-wire circuit is the simplest way to measure the temperature of a Pt100 element (see fig. 3.15). In this case it was measured over the voltage drop from an ohmic resistor. A CENTER 300 thermometer, a MS8215/8217 series multimeter and a Manson NP-9600 series power supply were used for the measurement. The voltage U_1 was recorded with an 8-channel USB-data acquisition modul (HB628) from the H-Tronic enterprise.
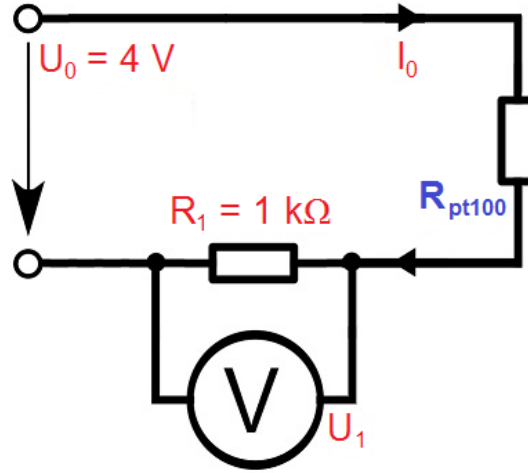
Figure 3.15.: The two-wire circuit is shown in this figure. The temperature was measured indirectly with the voltage drop U_1 at the ohmic resistor R_1.

The following formula was used for the analysis of four temperature points:

$$U_1 = U_0 \left(1 + \frac{R_2}{R_1} \right)^{-1} \tag{3.6}$$

where $U_0 = (4.04 \pm 0.02)$ V and $R_1 = (989 \pm 5)$ Ω. The total error is combined of the statistical error of the random sample and the systematic error of the formula:

$$\Delta U_1 = \left| \left(1 + \frac{R_2}{R_1} \right)^{-1} \right| \Delta U_0 + \left| \frac{U_0}{R_1} \left(1 + \frac{R_2}{R_1} \right)^{-2} \right| \Delta R_2 + \left| \frac{U_0 R_2}{R_1^2} \left(1 + \frac{R_2}{R_1} \right)^{-2} \right| \Delta R_1 \tag{3.7}$$

The result of this measurement is summarized in table 3.6:

Table 3.6.: Result of the two-wire circuit measurement:

T [℃]   ...   temperature in ℃ ($\Delta T = \pm 1$ ℃)
U_1 [mV]   ...   voltage drop in mV

T [℃]	U_1 [mV]
-193	3864 ± 49
1	3615 ± 45
22	3593 ± 46
98	3490 ± 44

As one can see in fig. 3.16 the measurement was rather inaccurate. This happened probably because of the one-sided offset of the data acquisition modul (HB628).
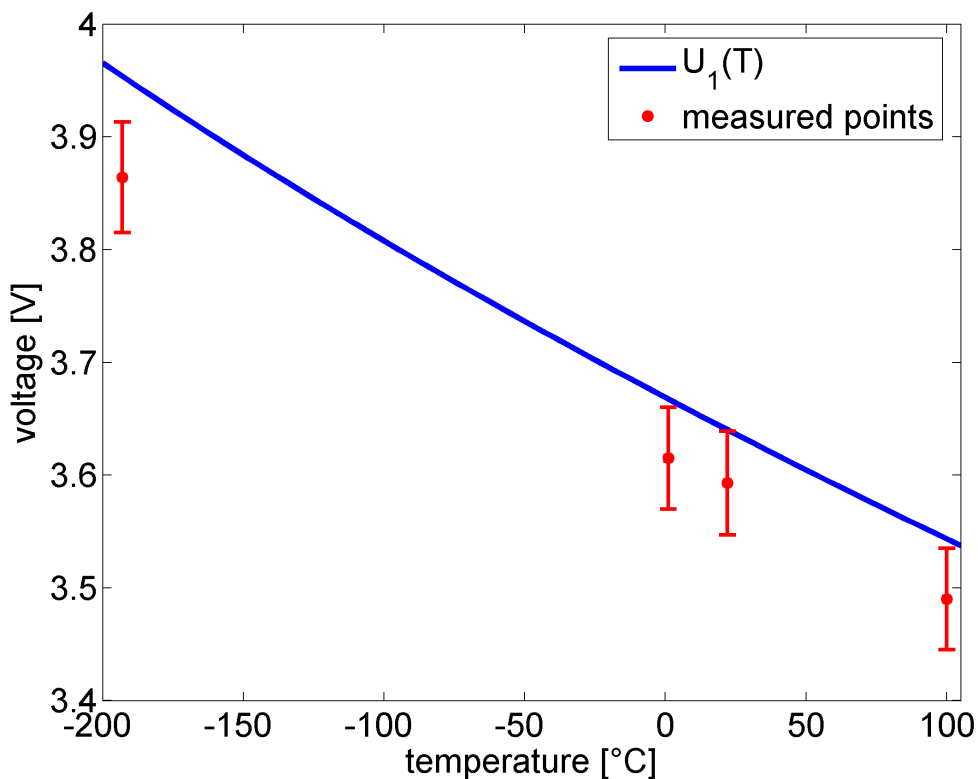
Figure 3.16.: Voltage-temperature characteristic for the two-wire circuit. The result is very inaccurate and the measured points are drifting in one direction.

3.3.3. Second Temperature Measurement Circuit

Another way to measure the temperature was to use a constant current source (see fig. 3.17) with a noninverting amplifier ($v = 50$). For temperatures greater than 0 °C, the resistance of the Pt100 element is greater than 100 Ω, which means a voltage above 5 V. Since the amplifier was only connected with a voltage of 5 V, the noninverting amplifier circuit could not be used for the temperature range over 0 °C. Here the temperature was measured directly via the voltage drop of the Pt100 element, since the interesting temperature region lies at low temperatures.
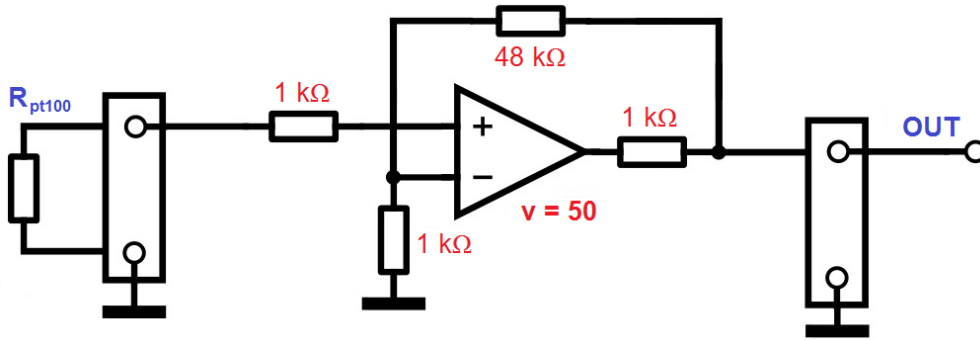
Figure 3.17.: The amplifier circuit is depicted in this figure. The amplification factor is 50. which reduces the error at lower temperatures.

The output voltage was again recorded with the 8-channel USB-data acquisition modul (HB628):

$$U_e = I_0 R_2 \tag{3.8}$$

$$U_e = \frac{U_a}{v} \tag{3.9}$$

with $I_0 = (1.00 \pm 0.01)$ mA. The total error is again combined of the statistical error of the random sample and the systematic error of the formulas:

$$\Delta U_e = \Delta I_0 R_2 + I_0 \Delta R_2 \tag{3.10}$$

$$\Delta U_e = \frac{\Delta U_a}{v} \tag{3.11}$$

The result of this measurement is summarized in the following table 6.5:

Table 3.7.: Result of the amplifier circuit measurement:

$T\ [°C]$ ...   temperature in °C $(\Delta T = \pm 1)$ °C
$U_e\ [mV]$ ...   input voltage from the Pt100 element in mV

$T\ [°C]$	$U_e\ [mV]$
-193	22 ± 1
1	95 ± 7
21	100 ± 8
98	129 ± 10

As one can see in fig. 3.18, the amplifier measurement is very accurate for low temperatures, with a small margin for error. Also, the other temperature points lie within the temperature-voltage characteristic of the error bar.
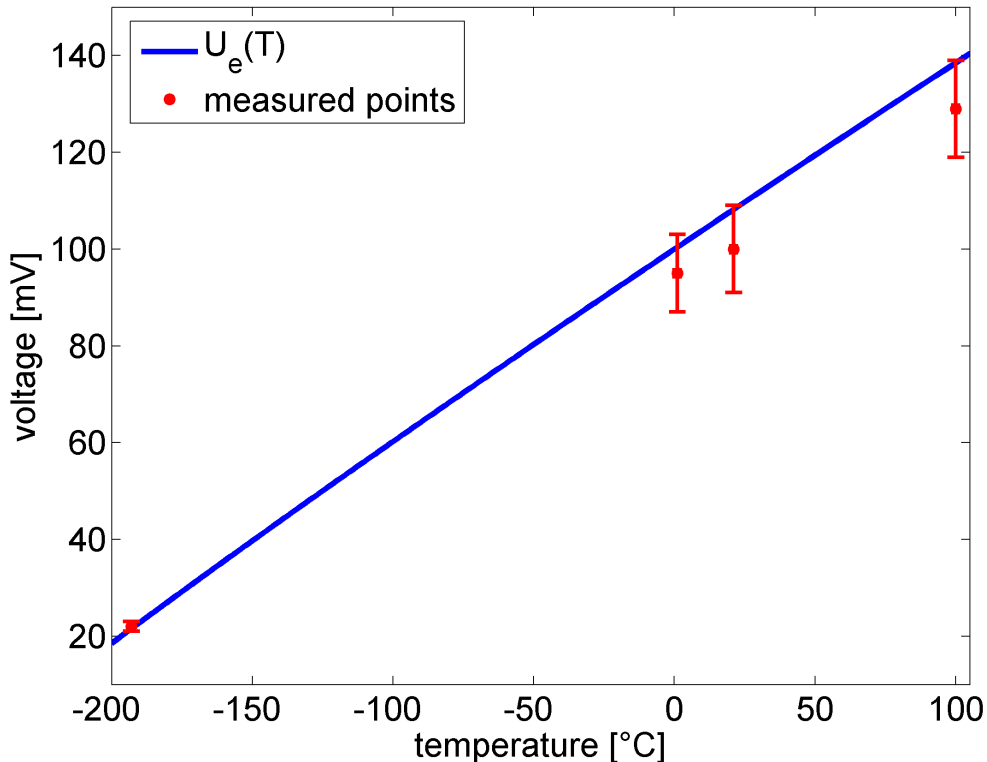
Figure 3.18.: Voltage-temperature characteristic for the amplifier circuit. For low temperatures the measurement method is very accurate.

3.3.4. Temperature Measurements with Small and Large Loads

Measurements for the end temperature reached with the cold head were carried out for small and large loads. The purpose was to simulate the cooling process of the sample in the main chamber and to obtain the lowest temperatures for different loads.

To fix the Pt100 element and the Type-K thermocouple at the second stage of the cold head, a small copper disc with a diameter of 54 mm, a thickness of 13 mm and a mass of 265 g was used (small load). The large load was made out of a copper cylinder connected to a copper string. The end of the copper string was attached to aluminum parts, where the Pt100 element and the Type-K thermocouple were

attached.

For small loads there is a way to estimate the time evolution of the temperature. First of all the cooling power as a function of the temperature (see fig. 3.19), which was taken from the manual[35], is needed:

$$\dot{Q}(T) = 12.0742 \cdot \ln(T) - 27.7353 \tag{3.12}$$
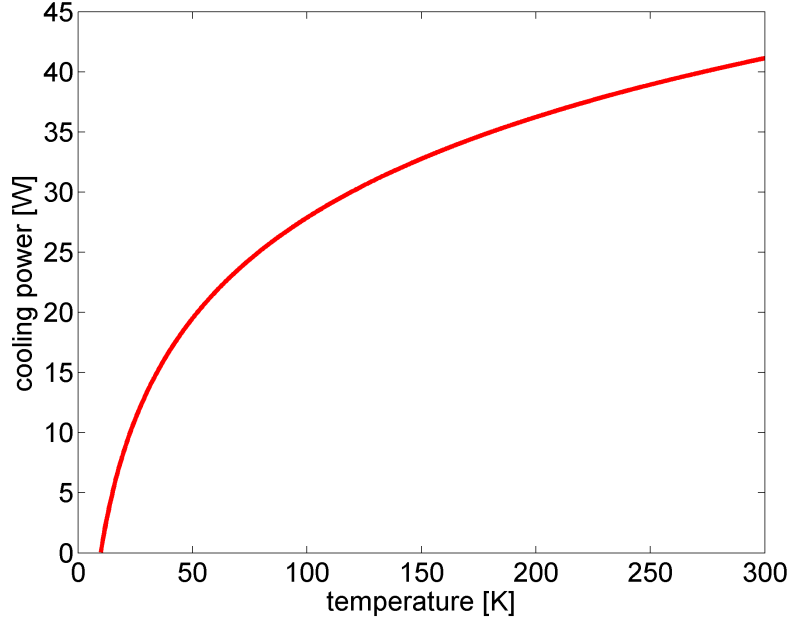
Figure 3.19.: Cooling power as a function of the temperature for the cold head RGD1245. For 10 K the cooling power is 0 W and for 300 K it is 40 W.

Out of the relation $\dot{Q}(T) = -c_p m \dot{T}$, a simple differential equation has to be solved:

$$dt = -c_p m \frac{dT}{\dot{Q}(T)} \tag{3.13}$$

where c_p is the specific heat capacity and m is the mass. The solution to this differential equation is:

$$t = 0.8 \cdot c_p m \text{Ei}(\ln(T) - 2.3) + C \tag{3.14}$$

where Ei(z) is the exponential integral function

$$\text{Ei}(z) = -\int_{-z}^{\infty} \frac{e^t}{t} dt \tag{3.15}$$

The constant C is determined by the fact that $T(0) = 300$ K holds in the beginning of the cooling process. The following parameters were used for the copper disc:

$c_p = 0.382$ Jg^{-1}K^{-1} and $m = 265$ g. Finally, we obtain the following function for the cooling time of the copper disc:

$$t = 1090 - 83 \cdot \mathrm{Ei}(\ln(T) - 2.3) \tag{3.16}$$

The theoretical estimation of the cooling curve for the copper disc is shown in fig. 3.20.

The temperature measurements were done with the amplification circuit, an EU-ROTHERM temperature control device and a Type-K thermocouple as a reference. For lower temperatures, the slope for the Type-K thermocouple is bigger than for the other measurements. The reason for that is that temperature measurements at low temperatures are getting inaccurate for the Type-K thermocouple, and the temperature measurement is limited to 70 K. The Pt100 element is able to measure lower temperatures, but is also limited. In the case of the small load, an end temperature of 35 K was reached (see fig. 3.20).
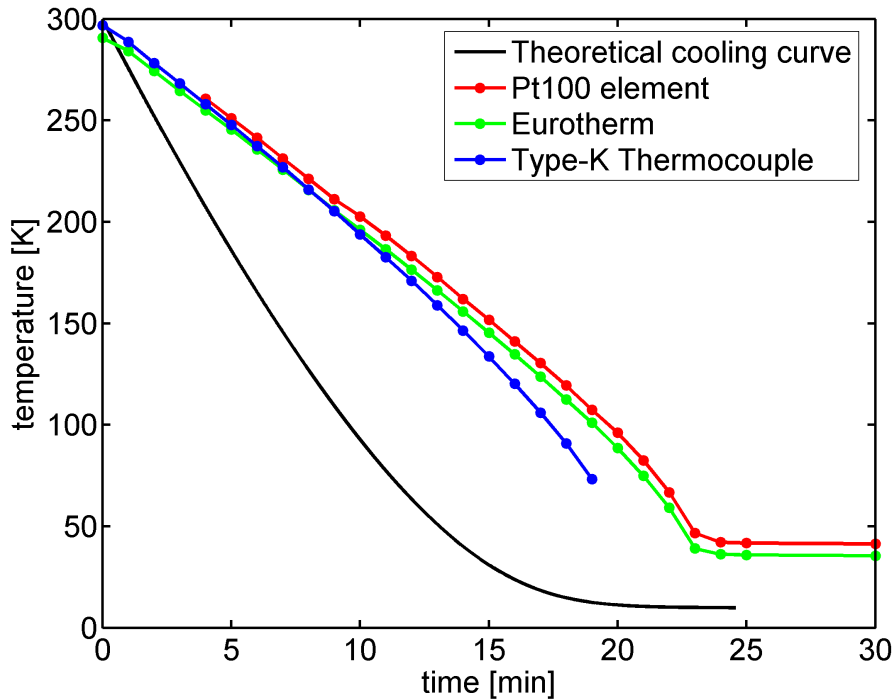
Figure 3.20.: Temperature measurements for the small copper disc. An end temperature of 35 K was measured with the Pt100 element. Also the theoretically estimated cooling curve is drawn.

For the large load, a single copper string with a length of 0.5 m was compared to a double copper string with a length of 0.57 m (see fig. 3.21). In both measurements the Type-K thermocouple was used again as a reference. For low temperatures the

amplifier circuit was used to obtain the end temperature with the Pt100 element. In the time range of (0-70) min, the Type-K thermocouple measurement has the same slope as the amplifier circuit measurement. The data of the first 66 min are measured with the Type-K thermocouple and the remaining data results from the amplifier circuit measurement after an offset of 7 K was subtracted.

For the single copper string an end temperature of 88 K and for the double copper string an end temperature of 56 K was achieved. As expected the copper string with the larger cross section reaches the lower end temperature, because it determines the heat transportation. The larger the cross section, the better the heat conduction is through the material. Also the end temperature is reached faster for the double copper string than for the single copper string.
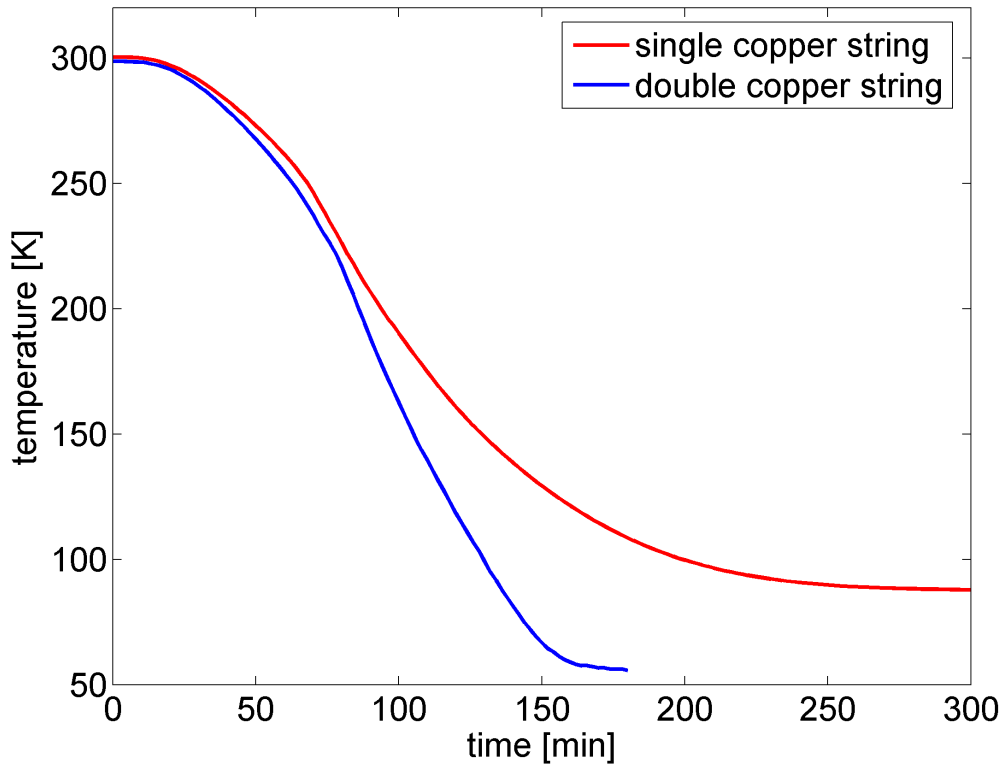
Figure 3.21.: Temperature measurement with large load. For the single copper string an end temperature of 88 K and for the double copper string an end temperature of 56 K was reached.

In fig. 3.22 the cooling rate for both copper strings is shown, which is simply the slope of the temperature measurements in fig. 3.21. The maximum for the double

copper string 2.8 K min^{-1} is reached after 79 min. For the single copper string, the maximum 2 K min^{-1} is reached after 88 min. This is another indication for better heat transport in the double copper string.
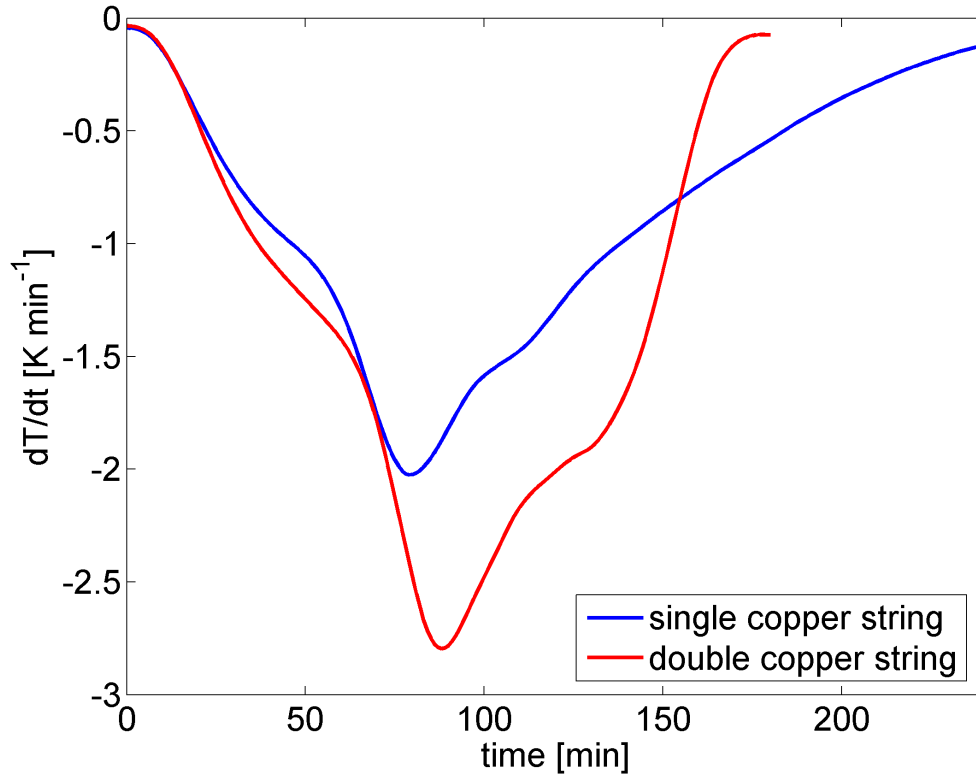
Figure 3.22.: Time dependent cooling rate of the single and the double copper string. The maximum for the single copper string is 2 K min^{-1} and for the double copper string 2.8 K min^{-1}.

3.3.5. FEM Analysis of the Copper String

The cooling process of the copper string was analyzed theoretically by the FEM described in section 2.5. The schematic model of the investigation object is depicted in fig. 3.23. It is defined by a rectangular basic domain Ω and four boundaries $R_1 - R_4$. It is assumed that the thickness t of the copper string is negligibly small in comparison to the other dimensions. The parameters for the heat equation in 2.81 for copper were chosen to be:

- $\rho = 8.92$ gcm^{-3}

- $c_p = 0.38$ Jg^{-1}K^{-1}

- $\lambda = 4$ Wcm^{-1}K^{-1}
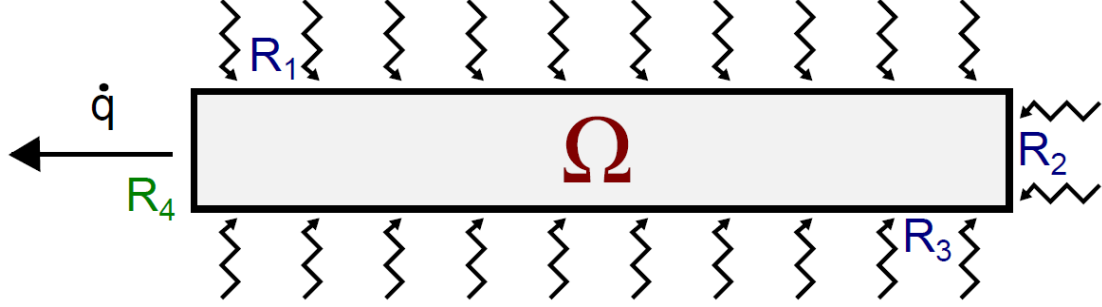
Figure 3.23.: Schematic FEM model of the copper string. On the boundary R_4 the cooling takes place. The copper string is exchanging heat radiation with the vacuum walls on the boundaries $R_1 - R_3$.

On the boundaries R_1-R_3 the exchange of heat radiation with the vacuum walls is described by the following Cauchy boundary condition:

$$-\lambda \left(\frac{\partial T}{\partial x} n_x + \frac{\partial T}{\partial y} n_y \right) = \alpha_{rad.}(T)(T - T_w) \tag{3.17}$$

$$\alpha_{rad.}(T) = \epsilon_{cu}\sigma(T + T_w)(T^2 + T_w^2) \tag{3.18}$$

where n_x and n_y are the components of the surface normal vector. $T_w = 300$ K is the temperature of the vacuum walls, $\epsilon_{cu} = 0.78$ the emission degree of copper and σ the Stefan-Boltzmann constant. The cooling is described by the following Neumann boundary condition at the boundary R_4:

$$-\lambda \left(\frac{\partial T}{\partial x} n_x + \frac{\partial T}{\partial y} n_y \right) = \frac{\dot{Q}(T)}{A} \tag{3.19}$$

where A is the area and $\dot{Q}(T)$ the cooling power from eq. 3.12.[36]
At first the temperature at the end of the copper string as a function of time was analysed (see fig. 3.24). The result was that the longer and thinner the copper string is, the longer the cooling of the sample takes. The reason is that for a larger cross section a larger amount of heat can be transported away through the matter by heat conduction.
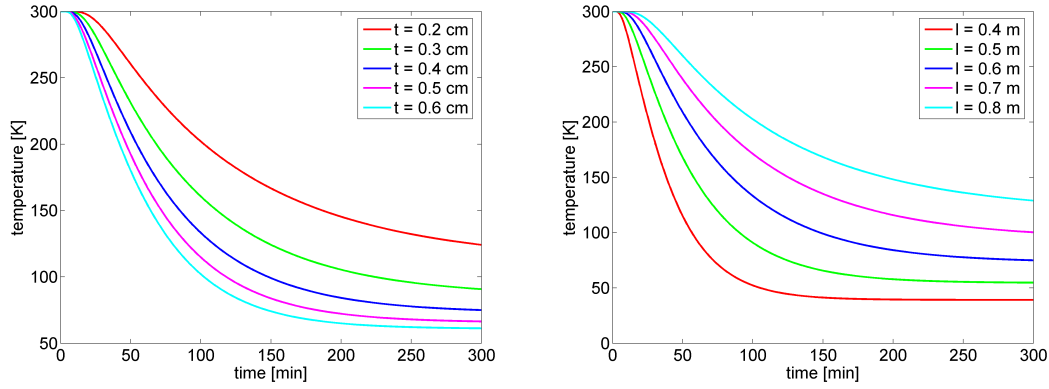
Figure 3.24.: Time evolution of the temperature for different thicknesses t (left) and lengths l (right). The thinner the copper string is, the longer the cooling takes. The length was chosen to be $l = 0.6$ m (left). The longer the copper string is, the longer the cooling takes. The thickness was chosen to be $t = 0.4$ cm (right).

As a second simulation the end temperature was analyzed as a function of the thickness t and length l (see fig. 3.25). The end temperature decreases with increasing thickness t at a constant length l and is proportional to t^c. c ranges from -1.12 to -0.81 with increasing length l. The end temperature increases with increasing length l at a constant thickness t and is proportional to l^c. c ranges from 1.52 to 1.90 with increasing thickness t.
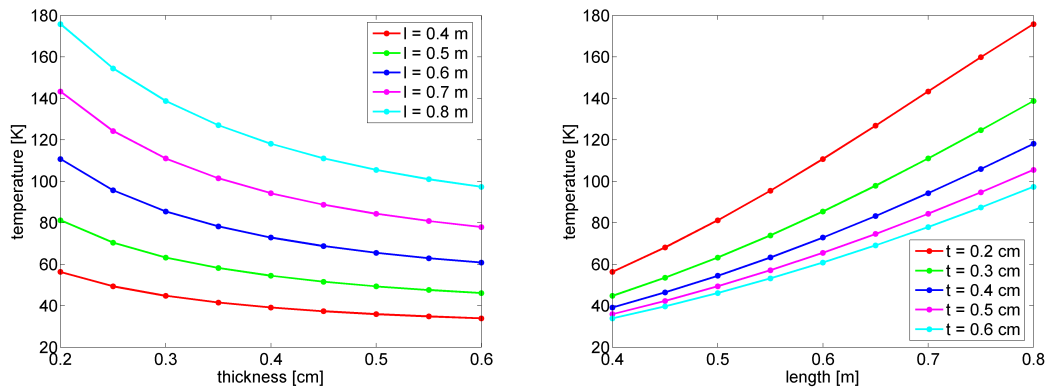
Figure 3.25.: Analysis of the end temperature as a function of thickness t (left) and length l (right). The end temperature is proportional to t^c where c ranges from -1.12 to -0.81 with increasing length (left). The end temperature is proportional to l^c where c ranges from 1.52 to 1.90 with increasing thickness (right).

4. Elastic Scattering Measurements

This section deals with the fundamental proceeding for elastic scattering measurements and shows how the nozzle temperature of the gas T_N is determined from TOF measurements. Both measurements are performed with the previously described HAS apparatus (see fig. 3.1). The helium beam is generated by a supersonic expansion of heliumgas ($p = 50$ bar) through a nozzle with a diameter of 10 μm. The central part of the beam is selected by a skimmer with a diameter of 380 μm. With an energy spread of $\Delta E/E \approx 2$ %, the helium beam is nearly monoenergetic. After the helium particles are scattered from the surface of the sample, they are detected by a QMS device.[11]

The sample itself was a Sb(111) single crystal in the shape of a disc. The diameter was 15 mm and the thickness 2 mm. It was mounted on the sampleholder, which was attached to a manipulator with six degrees of freedom. The surface temperature was measured with a Type-K thermocouple. The cleaning of the surface was done by a Ar$^+$-sputtering process and an annealing process. After a few rounds the surface is uncontaminated and flattened.[11]
The topmost layer of the Sb(111) single crystal has a sixfold symmetry. Thus, only the directions $< 10 >$ and $< 11 >$ on the surface have a different spacing of atoms. The azimuthal alignment of the crystal was checked with a LEED measurement. The scattered intensity of helium atoms was then scanned as a function of the initial scattering angle Θ_i. In this angular scan, the zero order diffraction peak occurs at an incident angle of $\Theta_i = 45.75°$. Also first and second order diffraction peaks are observed.[11]

4.1. Determination of the Real Nozzle Temperature

The nozzle temperature of the gas T_N was measured with a Pt100 element that is directly attached to the helium source. It is connected to an EUROTHERM temperature control device, which displays the temperature digitally in units of K.

The main disadvantage is that this temperature is inaccurate. Therefore another method had to be found to determine the exact nozzle temperature of the gas. The solution is to use a TOF measurement at the specular peak (0th order diffraction peak) to determine the real nozzle temperature of the gas T_N accurately. The flight path l at which the helium particles are traveling from the source to the detector is 1.65 m. To obtain the flight time t_0 of the helium atoms, a Gaussian fit was used for the TOF data (see fig. 4.1):

$$g(t) = h \exp\left(-\left(\frac{t - t_0}{\Delta t}\right)^2\right) \qquad (4.1)$$

The coefficients h and Δt are the height and the width of the Gauss peak respectively. Knowing the flight time t_0, the most likely velocity v of the helium atoms can be calculated wit $v = \frac{l}{t_0}$. When the equations 2.11 and 2.13 are combined and transformed the nozzle temperature of the gas, T_N can be finally computed:

$$T_N = \frac{mv^2}{5k_B} = \frac{ml^2}{5k_B t_0^2} \qquad (4.2)$$
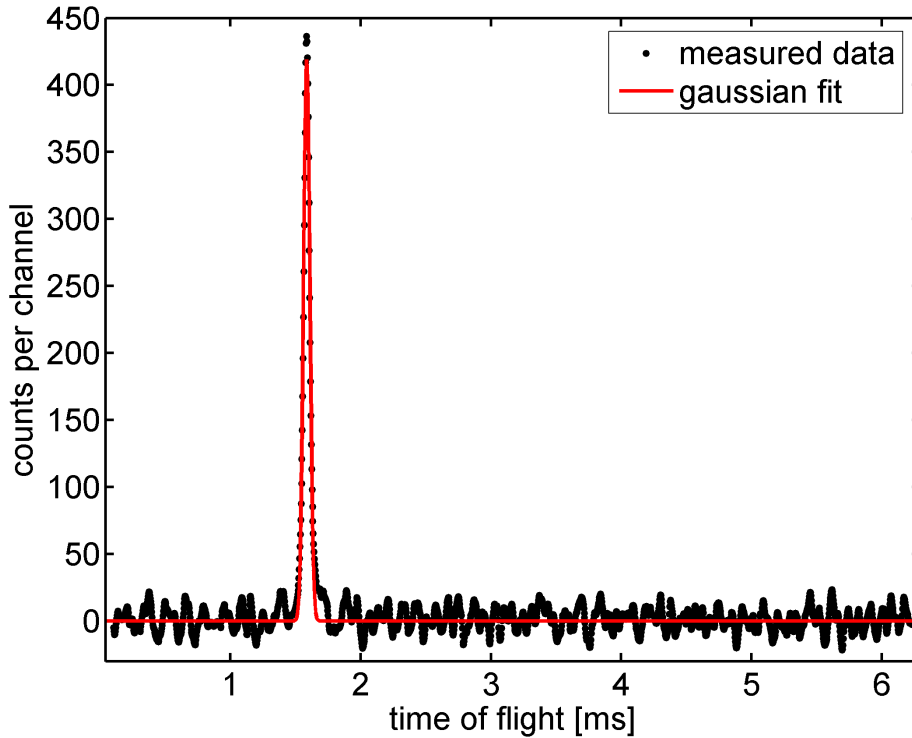
Figure 4.1.: Typical TOF measurement performed at the specular peak at 104.2° for 300 s. From a Gaussian fit, the most likely flight time t_0 is determined to calculate furthermore the nozzle temperature of the gas T_N.

In fig. 4.1 an example of a TOF measurement is depicted. It was recorded at an incident angle of $\Theta_i = 104.2°$ where the specular peak is positioned. To obtain good statistics the scan was done for 300 s. The Gaussian fit yields the following coefficients h, Δt and flight time t_0:

- $h = (419 \pm 3)$ cps

- $\Delta t = (0.034 \pm 0.017)$ ms

- $t_0 = (1.586 \pm 0.001)$ ms

One notices that the flight time t_0 can be determined very accurately because of the very sharp Gauss peak. By plugging in the flight time into equation 4.2, a nozzle temperature of the gas of $T_N = (104.16 \pm 0.13)$ K is yielded.

5. Structure and Properties of Sb(111)

The group V semimetal antimony (Sb) is briefly described in this section. The crystal structure of Sb is an A7 structure (R$\bar{3}$m space group) and can be described by a rhombohedral unit cell with two atoms in it. Another way to describe the structure is a conventional hexagonal cell consisting of six atoms. The layers are stacked here in the sequence ABCABC. The bulk structure is built of puckered bilayers perpendicular to the [111] direction (see fig. 5.1). The bonds are separated into strong intrabilayer bonds with a length of 2.9 Å and weaker interbilayer bonds with a length of 3.4 Å.[7]

There are four ways to describe the surface: The indices can either be rhombohedral, three or four hexagonal, or pseudocubic. For the description of the Sb(111) surface, three hexagonal indices are used. In fig. 5.1 the rhombohedral structure is depicted. The length of the basis vector of the unit cell is $a = 4.507$ Å. The topmost layer has a sixfold symmetry. That is why the surface has only two low-index directions with different distances of the atoms: The $< 10 >$ and the $< 11 >$ direction.[7]
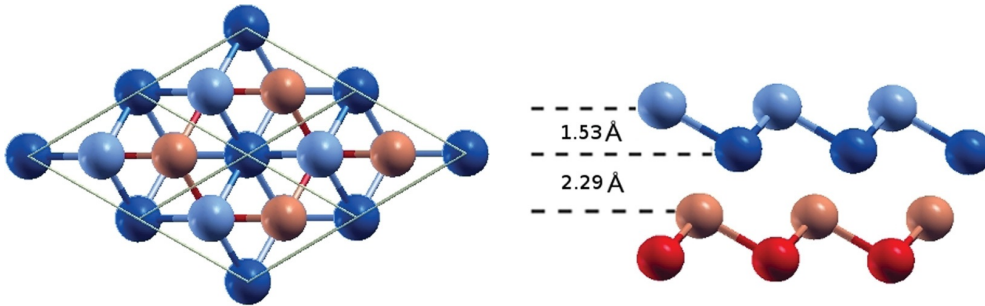
Figure 5.1.: The rhombohedral surface structure of Sb(111) (left) and the side view of the bulk structure is shown (right). Within the bilayers there are strong covalent intrabonds beneath the weaker van der Waals interbonds.[7]

6. Results and Discussion

This section deals with the experimental results of the elastic HAS measurements, which were performed on a Sb(111) crystal surface. It is shown how the angular scan measurements are prepared for further calculations. Two angular scans with about the same nozzle temperature of the gas but different scattering directions and two angular scans with the same scattering direction but different nozzle temperatures of the gas are compared to each other respectively. Moreover, the surface lattice constant of the Sb(111) sample is obtained from the angular positions of the diffraction peaks. Additionally, two CC-programs were tested on the LiF(001) surface structure. The GR-method calculations of García[15] serve as a reference.

6.1. Angular Scan Fitting Procedure

An angular scan consists of discrete data points, which are separated by a fixed angular step width Θ_{step}. The scan range Θ_{range}, step width Θ_{step} and measure time for one measured data point t_{step} is thereby set up with certain MATLAB routines. For further calculations the measured data are fitted with Gauss functions of the form:

$$g(\Theta) = h \exp\left(-\left(\frac{\Theta - \Theta_0}{\Delta\Theta}\right)^2\right) \tag{6.1}$$

The different Θ_0 are the angular positions of all occuring diffraction peaks. h and $\Delta\Theta$ are the height and the width of the Gauss peak respectively. Another interesting quantity is the area under the Gauss function, which is simply given by:

$$A = \sqrt{\pi}h\Delta\Theta \tag{6.2}$$

As an example the Gauss fit in fig. 6.1 is regarded. It shows a first order diffraction peak from an angular scan in the direction of $< 10 >$. The temperature of the sample is $T_{Sb} = 120$ K and of the nozzle $T_N = 104.2$ K. The stepwidth was chosen to be $\Theta_{step} = 0.1°$. The time for one measured data point was $t_{step} = 20$ s. The following coefficients are yielded by the Gaussian fit:

- $h = (3646 \pm 75)$ cps

- $\Delta\Theta = (0.340 \pm 0.008)°$

- $\Theta_0 = (56.050 \pm 0.005)°$

The area under the curve is then $A = (2199 \pm 98)$ cps°. For an ideal measurement the diffraction peaks would become δ-peaks at a sample temperature of $T_N = 0$ K because of the monochromatic helium beam. The energy spread of the supersonic beam and the dynamic of the surface atoms at higher sample temperatures broaden up the peak. Thus the area under the Gauss peaks is an indication for the number of helium atoms which are scattered from the surface at a certain angular position.
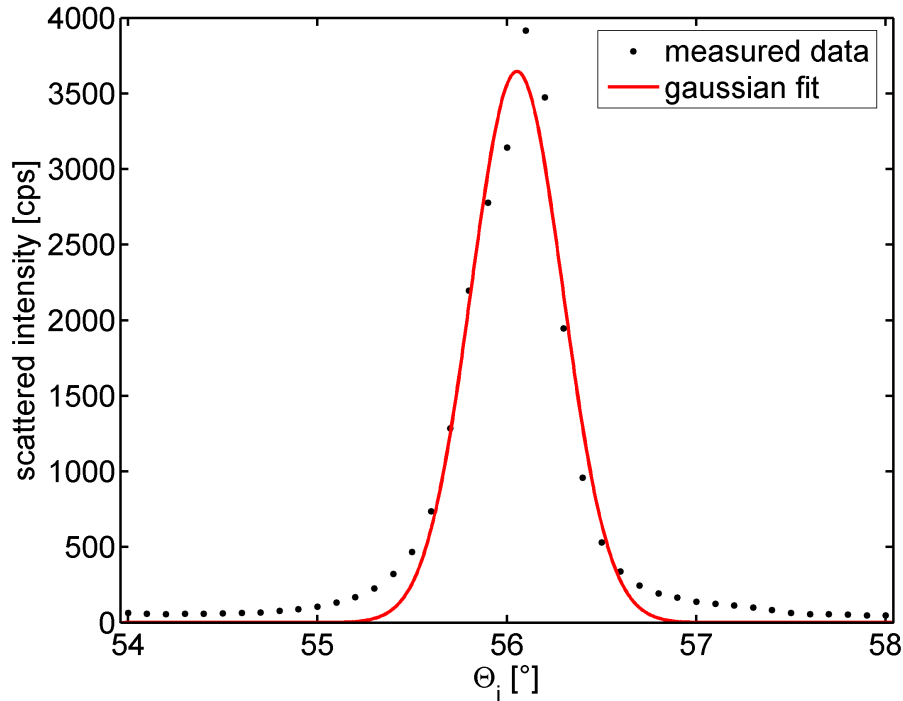
Figure 6.1.: Gaussian fit of a first order diffraction peak. The angular position Θ_0, peak height h and peak area A can be determined.

6.2. Angular Scans with about the Same Incident Energy

Two angular scans with about the same nozzle temperature but different scattering directions are compared with each other (see fig. 6.2). The incident energy of

the helium atoms is strongly related to the nozzle temperature of the gas T_N (see equ. 2.22). Here only diffraction peaks up to the first order are considered. The properties of the angular scans in fig. 6.2 are given in tab. 6.1.

Table 6.1.: Properties of the angular scans with about the same nozzle temperature but different scattering directions:

direction	...	particle scattering direction
T_{Sb} [K]	...	temperature of the sample in K
T_N [K]	...	temperature of the nozzle in K
E_i [meV]	...	incident energy of the helium atoms in meV
Θ_{step} [°]	...	angular step size in degrees
t_{step} [s]	...	measure time for one data point in s

property	1st angular scan	2nd angular scan
direction	< 10 >	< 11 >
T_{Sb} [K]	120	121
T_N [K]	104.2	105.2
E_i [meV]	22.47	22.68
Θ_{step} [°]	0.1	0.1
t_{step} [s]	20	10

The measured data was fitted by Gaussian functions (see fig. 6.2). The results for the angular positions, peak heights and peak areas are given in tab. 6.2.

Figure 6.2.: Two angular scans with nearly the same incident energy. The left one was measured in the < 10 > and the right one in the < 11 > scattering direction.

Table 6.2.: Comparison of the angular scans with about the same nozzle temperature but different scattering directions:

order	...	order of the peak (l for left and r for right)
Θ_i [°]	...	angular position in degrees
h [cps]	...	peak height in cps
A [cps°]	...	peak area in cps°

order	Θ_i [°]	h [cps]	A [cps°]
0.	45.710±0.003	7093±127	1227±46
1.(l)	35.160±0.003	3443±96	1269±76
1.(r)	56.050±0.005	3646±75	2199±98
0.	45.750±0.001	11550±83	2577±41
1.(l)	27.080±0.010	1136±52	619±61
1.(r)	64.020±0.010	1435±45	1034±70

An important observation is that in the direction of $< 11 >$ the first order peaks are further away from the specular peak than in the direction of $< 10 >$. The reason for this behaviour is that the lattice plane distances in the $< 11 >$ direction are smaller than for the $< 10 >$ direction. Since a small distance of lattice planes leads to higher reciprocal lattice vectors, the first order peaks move further away from the zero order peak (see also equ. 2.33).

6.3. Angular Scans in the $< 10 >$ Scattering Direction

Two angular scans in the scattering direction $< 10 >$ at different incident energies are compared with each other (see fig. 6.3). From the nozzle temperature T_N the incident energy of the helium atoms is obtained (see equ. 2.22). Here only diffraction peaks up to the second order are considered. The properties of the angular scans in fig. 6.3 are given in tab. 6.3.

Table 6.3.: Properties of the angular scans in the scattering direction $< 10 >$ at different incident energies:

direction   ...   particle scattering direction
T_{Sb} [K]   ...   temperature of the sample in K
T_N [K]   ...   temperature of the nozzle in K
E_i [meV]   ...   incident energy of the helium atoms in meV
Θ_{step} [°]   ...   angular step size in degrees
t_{step} [s]   ...   measure time for one data point in s

Property	1st angular scan	2nd angular scan
direction	$< 10 >$	$< 10 >$
T_{Sb} [K]	298	120
T_N [K]	74.3	104.2
E_i [meV]	16.02	22.47
Θ_{step} [°]	0.1	0.1
t_{step} [s]	130	20

The measured data was fitted by Gaussian functions (see fig. 6.3). The results for the angular positions, peak heights and peak areas are given in tab. 6.4.
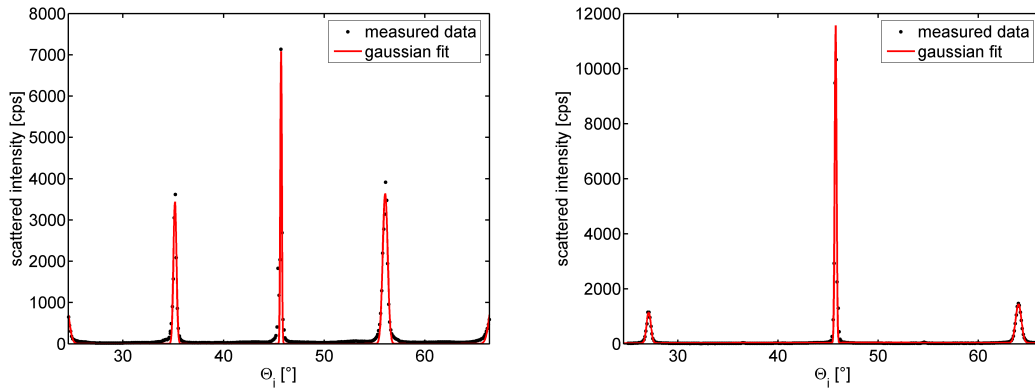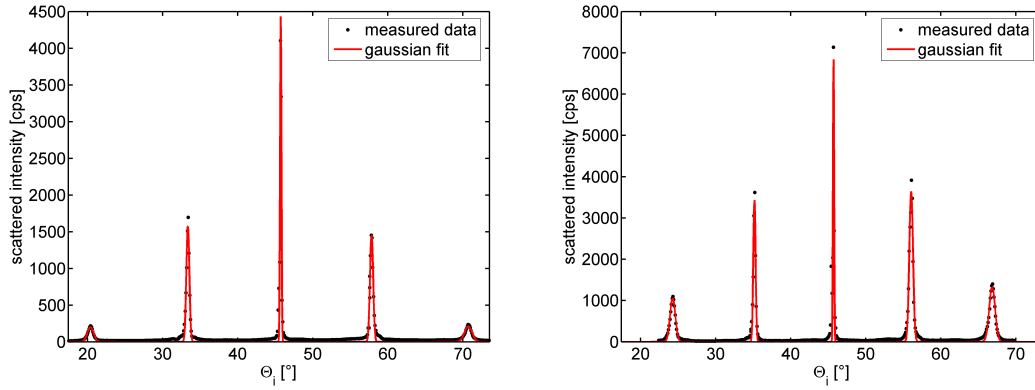

Figure 6.3.: Two angular scans in the scattering direction $< 10 >$. The left one was recorded at an incident energy of 16.02 meV and the right one at an incident energy of 22.47 meV.

Table 6.4.: Comparison of the angular scans in the scattering direction $< 10 >$ at different incident energies:

order	...	order of the peak (l for left and r for right)	
Θ_i [°]	...	angular position in degrees	
h [cps]	...	peak height in cps	
A [cps°]	...	peak area in cps°	

order	Θ_i [°]	h [cps]	A [cps°]
0.	45.740±0.003	4474±52	937±24
1.(l)	33.360±0.003	1588±33	780±35
1.(r)	57.840±0.005	1456±32	749±34
2.(l)	20.380±0.055	200±23	207±51
2.(r)	70.730±0.053	211±21	268±57
0.	45.710±0.003	7093±127	1227±46
1.(l)	35.160±0.003	3443±96	1269±76
1.(r)	56.050±0.005	3646±75	2199±98
2.(l)	24.270±0.023	1054±62	918±117
2.(r)	66.850±0.020	1328±59	1306±125

An important fact is that the diffraction peaks are moving nearer to the specular peak for higher energies. An explanation for this is that a higher energy yields a higher incident wavevector of the incoming particles and thus the diffraction peaks are moving nearer to the zero order peak (see also equ. 2.33).

6.4. Double Peak for Zero Order Diffraction

In fig. 6.4 an interesting feature is shown at the specular peak. The zero order diffraction peak is split into a double peak (see fig. 6.4 left). The reason for this behaviour is either a step edge on the surface or a local damage of the sample surface caused by excessive heating.

An interesting fact is how the properties of the Gauss fit changes if the data point (in fig. 6.4 right drawn magenta) that splits the specular peak is neglected. It is shown that the height as well as the area under the Gauss peak increases.
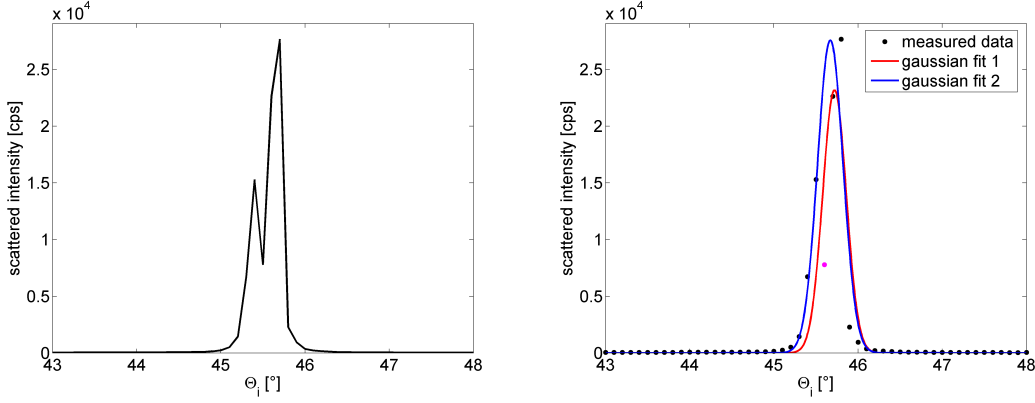
Figure 6.4.: The zero order diffraction peak is split into a double peak (left). The red and blue lines represent Gaussian fits with and without neglection of the data point (magenta) respectively (right).

6.5. Determination of the Lattice Constant

From the angular positions of the different diffraction peaks it is possible to determine the surface lattice constant. At first the norm of the reciprocal lattice vectors G has to be calculated by transforming equ. 2.33:

$$G = 2k_i \cos\left(\frac{\Theta_{SD}}{2}\right) \sin\left(\frac{\Theta_{SD}}{2} - \Theta_i\right) \tag{6.3}$$

The incident wavevector k_i is determined from the incident energy of the incoming particles E_i, which is calculated from the nozzle temperature T_N. The higher the diffraction order, the higher the norm of the reciprocal lattice vector. The relation $d = \frac{2\pi}{G}$ yields the distance of the lattice planes standing normal on the surface (see fig. 6.5). Considering the red triangle in fig. 6.5 for the real space, the lattice constant is calculated by

$$a = \frac{4\pi}{n\sqrt{3}G} \tag{6.4}$$

n is representing the diffraction order. For the calculation the two angular scans in fig. 6.3 have been considered. The results are given in tab. 6.5:
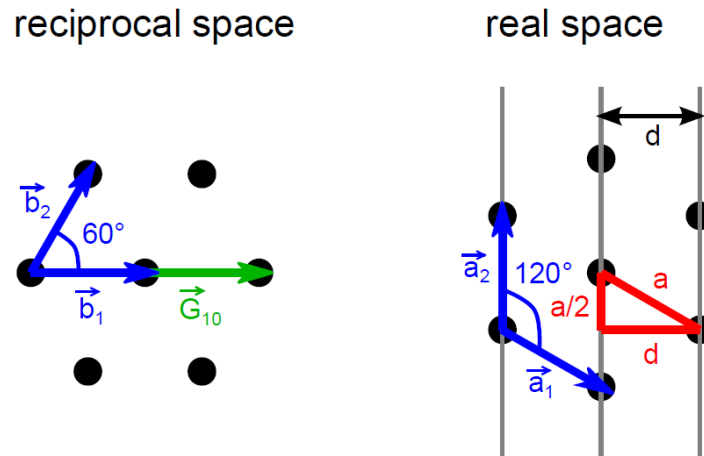
Figure 6.5.: Surface lattices in reciprocal space and real space respectively for the < 10 > scattering direction. The lattice constant is obtained from the red triangle.

Table 6.5.: Calculation of the lattice constant:

Θ_i [°]   ...   angular position in degrees
G [Å^{-1}]   ...   norm of the reciprocal lattice vector in Å^{-1}
a [Å]   ...   lattice constant in Å

Θ_i [°]	G [Å^{-1}]	a [Å]
33.370±0.003	1.66±0.03	4.38±0.08
57.850±0.005	1.62±0.05	4.48±0.14
20.390±0.053	3.31±0.03	4.39±0.04
70.740±0.055	3.26±0.06	4.45±0.08
35.200±0.003	1.67±0.04	4.33±0.10
56.090±0.005	1.64±0.06	4.42±0.15
24.310±0.023	3.34±0.03	4.34±0.04
66.890±0.020	3.30±0.07	4.40±0.09
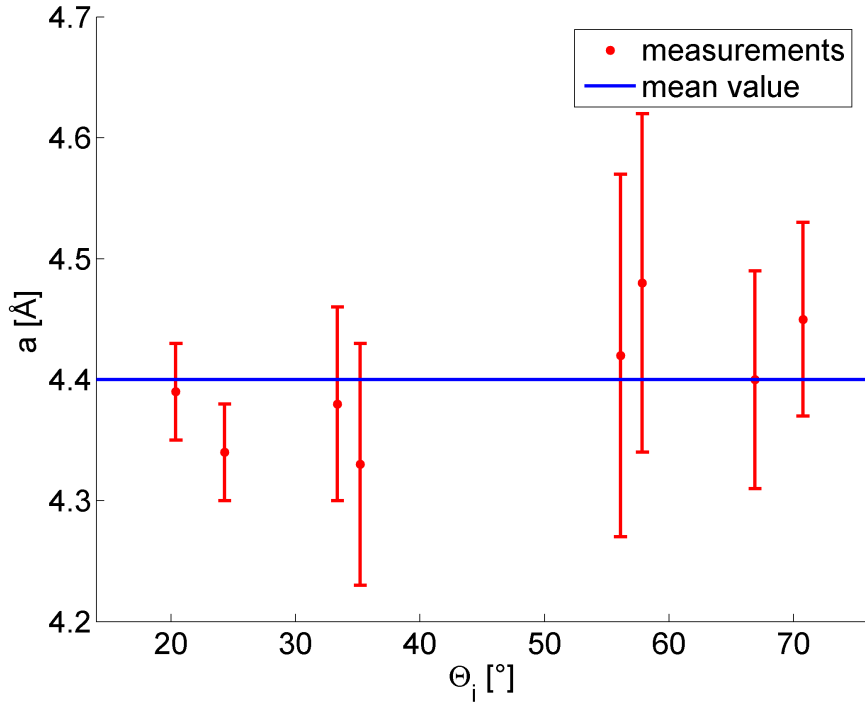
Figure 6.6.: Calculated lattice constants for different angular positions. The average value is at $a = 4.40$ Å.

In fig. 6.6 the lattice constants from tab. 6.5 are shown for the observed incident angles Θ_i. If the average is taken over the calculated lattice constants, it yields $a = 4.40$ Å. The literature value is going to be 4.30 Å[37].

6.6. Close Coupling Test Results

Two Close Coupling algorithms were tested on the surface structure of LiF(001). It has a square lattice structure with one Li-atom and one F-atom in the basis. The lattice constant is $a = 2.84$ Å. The shape function of the crystal surface structure of LiF(001) was chosen to be:

$$\xi(\vec{R}) = \frac{\xi_0}{2} \left(\cos\left(\frac{2\pi X}{a}\right) + \cos\left(\frac{2\pi Y}{a}\right) \right) \tag{6.5}$$

where ξ_0 is the corrugation amplitude and $\vec{R}$ is a lattice vector on the crystal surface.[27]
The program by Dr. A. Kaufhold from 1996 is based on the predictor-corrector Numerov algorithm written in TURBO-PASCAL. The interaction potential is a Lennard-Jones-Devonshire potential model. The self written program on the

other hand is based on the Coupling Channels method originally proposed by Liebsch and Harris[29]. Here the interaction potential is a Morse corrugated potential model. More details on the programs are given in the Appendix. As reference values serve the GR-method calculations from García, who used a Hard-Corrugated-Wall model for the surface structure.[15] To compare the own program with the calculations from García, the attractive part of the Morse corrugated potential was neglected.

The procedure of the computation is as follows. The corrugation amplitude was changed till the scattering amplitudes of the different channels are approximately equal to the literature values by García. Then the corresponding corrugation amplitude is obtained. The results are given in tab. 6.6. The scattering amplitudes are nearly the same for all calculations, but the corrugation amplitudes are marginally different. The reason for this behaviour is that the first two algorithms use an interaction potential with neglection of the attractive part, whereas in the third and fourth calculation the attractive part is taken into account in the interaction potential.

Table 6.6.: Close Coupling test results:

channel   ...   scattering channels
    1   ...   GR-method values from García
    2   ...   Own CC program (attractive part neglected)
    3   ...   CC program from Dr. A. Kaufhold
    4   ...   Own CC program
    ξ_0 ...   corrugation amplitude in Å

channel	1	2	3	4
	$\xi_0 = 0.110$ Å	$\xi_0 = 0.115$ Å	$\xi_0 = 0.128$ Å	$\xi_0 = 0.135$ Å
I_{00}	181.3	181.1	181.5	181.9
I_{10}	112.8	114.6	113.3	113.1
I_{11}	65.8	67.8	66.5	67.3
I_{20}	12.1	10.6	11.2	11.0
I_{21}	6.2	5.5	6.0	6.0
I_{22}	0.5	0.4	0.5	0.5

7. Conclusion and Outlook

The main result of this thesis consists of the HAS measurements performed on the Sb(111) crystal surface. In order to compare the different angular scans, the measured data was fitted with Gauss functions as shown in section 6.1. Because of the surface lattice dynamics of the surface atoms at temperatures above 0 K and the energy spread of the helium beam, the Gauss peaks are broadened.

Two angular scans with about the same incident energy but different scattering directions ($< 10 >$ and $< 11 >$) in section 6.2 and two angular scans in the $< 10 >$ scattering direction but different incident energies (16.02 meV and 22.47 meV) in section 6.3 are compared with each other. In both cases the angular positions of the higher order diffraction peaks change. The lattice constant for the $< 11 >$ direction is smaller than for the $< 10 >$ direction. Thus the angular positions of the higher order peaks are further away from the specular peak for the $< 11 >$ scattering direction according to equ. 2.33. In the second case the incident wavevector changes with the incident energy. Consequently, the angular positions of the higher order diffraction peaks are further away from the specular peak for lower incident energies of the helium atoms according to equ. 2.33. From the angular positions of the higher order diffraction peaks, the surface lattice constant was determined to a=4.40 Å. Compared to the literature value of a=4.30 Å[37] the value is about 0.1 Å, too high.

The CC-program from Dr. A. Kaufhold and the self-written CC-program were successfully tested on GR-method calculations by García.[15] The scattering probabilities of the observed scattering channels are approximately the same in all cases. If the attractive part is neglected in the self-written program, the corrugation amplitude ($\xi_0 = 0.115$ Å) is comparable with that obtained by García ($\xi_0 = 0.110$ Å). If the attractive part of the interaction potential is taken into account, the corrugation amplitude increases. The CC-program of Dr. A. Kaufhold and the self-written CC-program result in corrugation amplitudes of $\xi_0 = 0.128$ Å and $\xi_0 = 0.135$ Å respectively.

The limiting circuit for the button heater limits the output voltage of the power supply to prevent the sample from damage through excessive heating. The varying ohmic resistors can be attached to other samples in the future. The mounting of a new venting valve makes it possible to vent the vacuum chamber with different gases like argon or nitrogen. If the vacuum chamber is vented with nitrogen, the

UHV pressure region is reached faster. The temperature measurements of the Cold Head showed that a double copper string has more advantages than a single copper string. The reached end temperature for the double copper string is lower and the cooling process is faster. The FEM calculations show the same behaviour. The end temperature decreases with decreasing length and increasing thickness. For future projects the cold head could be mounted onto the HAS apparatus to reach lower sample temperatures. Also the CC-algorithm could be adapted for the HAS machine used in this thesis and expanded for resonance effects of helium atoms onto crystal surfaces. Another interesting field of research would be measurements of atomic adsorption on crystal surfaces.

8. Bibliography

[1] P. Hofmann. *Surface Physics: An Introduction.* Springer, 2012.

[2] D.R. Miller. *Atomic and Molecular Beam Methods (ed. G. Scoles)*, volume 1, chapter Free Jet Source, pages 15–53. Oxford University Press, 1983.

[3] A. Tamtögl. PhD thesis, Technische Universität Graz, 2012.

[4] G. Wolken. Theoretical Studies of atomsolid elastic scattering: He+LiF. *J. Chem. Phys.*, 58:3047, 1973.

[5] M. Mayrhofer-Reinhartshuber. Master's thesis, Technische Universität Graz, 2010.

[6] http://webbook.nist.gov/chemistry/name-ser.html.

[7] D. Campi, M. Bernasconi and G. Benedek. Phonons and electron-phonon interaction at the Sb(111) surface. *Phys. Rev. B*, 86:075446, 2012.

[8] N. Balak. Master's thesis, Technische Universität Graz, 2009.

[9] P. Kraus. Master's thesis, Technische Universität Graz, 2011.

[10] E. Hulpke. *Helium Atom Scattering from Surfaces.* Springer, 1992.

[11] A. Tamtögl, M. Mayrhofer-Reinhartshuber, N. Balak, W.E. Ernst and K.H. Rieder. Elastic and inelastic scattering of He atoms from Bi(111). *J. Phys.: Condens. Matter*, 22:304019, 2010.

[12] A. Tamtögl, P. Kraus, M. Mayrhofer-Reinhartshuber, D. Campi, M. Bernasconi, G. Benedek and W.E. Ernst. Surface and subsurface phonons of Bi(111) measured with helium atom scattering. *Phys. Rev. B*, 87:035410, 2013.

[13] M. Mayrhofer-Reinhartshuber, A. Tamtögl, P. Kraus, K.H. Rieder and W.E. Ernst. Vibrational dynamics and surface structure of Bi(111) from helium atom scattering measurements. *J. Phys.: Condens. Matter*, 24:104008, 2012.

[14] P. Kraus, A. Tamtögl, M. Mayrhofer-Reinhartshuber, G. Benedek and W.E. Ernst. Resonance-enhanced inelastic He-atom scattering from subsurface optical phonons of Bi(111). *Phys. Rev. B*, 87:245433, 2013.

[15] N. García. The scattering of He atoms from a hard corrugated surface model using the GR method. *J. Chem. Phys.*, 67:897, 1977.

[16] K. Oura, V.G. Lifshits, A. Saranin, A.V. Zotov, M. Katayama. *Surface Science*. Springer, 2003.

[17] C. Kittel. *Introduction to Solid State Physics*. John Wiley & Sons, Inc., New York, 8th edition, 2005.

[18] H. Lüth. *Solid Surfaces, Interfaces and Thinfilms*. Springer, 4th ed. edition, 2001.

[19] A. Apfolter. Master's thesis, Technische Universität Graz, 2005.

[20] H.C.W. Beijerinck and N.F. Verster. Absolute intensities and perpendicular temperatures of supersonic beams of polyatomic gases. *Physica B+C*, 111:327, 1981.

[21] H. Pauly. *Atom, Molecule and Cluster Beams I*. Springer, 2000.

[22] D.J. Auerbach. *Atomic and Molecular Beam Methods (ed. G. Scoles)*, volume 1, chapter Velocity measurements by Time-of-Flight methods, pages 363–379. Oxford University Press, 1983.

[23] G. Boato. *Atomic and Molecular Beam Methods (ed. G. Scoles)*, volume 2, chapter Elastic Scattering of Atoms, pages 340–365. Oxford University Press, 1983.

[24] H. Hoinkes. The physical interaction potential of gas atoms with single-crystal surfaces, determined from gas-surface diffraction experiments. *Rev. of Mod. Phys.*, 52:933, 1980.

[25] G. Armand and J.R. Manson. An exact iterative solution of the atom-surface scattering problem for realistic potentials. *Surf. Sci.*, 119:L299, 1982.

[26] R.Martínez-Casado, B. Meyer, S. Miret-Artés, F. Traeger and Ch. Wöll. Diffraction patterns of He atoms from the MgO(100) surface calculated by the close-coupling method. *J. Phys.: Condens. Matter*, 19:305006, 2007.

[27] V. Celli, D. Eichenauer, A. Kaufhold and J.P. Toennies. Pairwise additive semi ab initio potential for elastic scattering of He atoms from the LiF(001) crystal surface. *J. Chem. Phys.*, 83:5, 1985.

[28] W.E. Baylis and S.J. Peel. A Predictor-Corrector Form of the Numerov method for coupled equations. *Comp. Phys. Comm.*, 25:7, 1982.

[29] A. Liebsch and J. Harris. Interaction of helium with a metal surface II. Coupled channels method and effect of out-of-plane scattering for Cu(110). *Surf. Sci.*, 123:355, 1982.

[30] Lecture notes by Prof. Sormann about the FEM.

[31] G. Bärwolff. *Numerik für Ingenieure, Physiker und Informatiker*. Elsevier, 2007.

[32] P. Steinke. *Finite-Elemente-Methode*. Springer, 2007.

[33] K. Jousten. *Handbook of vacuum technology*. WILEY-VCH, 2008.

[34] K. Irrgang, L. Michalowsky. *Temperaturmesspraxis mit Widerstandsthermometern und Thermoelementen*. Vulkan, 2003.

[35] Operating instructions for cold heads for cryogenerators of the company LEY-BOLD VAKUUM.

[36] H.D. Baehr, K. Stephan. *Wärme- und Stoffübertragung*. Springer, 2010.

[37] A. Tamtögl, M. Mayrhofer-Reinhartshuber, P. Kraus, W.E. Ernst. Surface Debye Temperature and Vibrational Dynamics of Antimony(111) from Helium Atom Scattering Measurements. *Surf. Sci.*, 617:225, 2013.

[38] F. Träger. Helium Atom Scattering from Oxide Surfaces. *Chem. Phys. Chem.*, 7:1006, 2006.

[39] Ph. Hofmann. The surfaces of bismuth: Structural and electronic properties. *Prog. in Surf. Sci.*, 81:191, 2006.

A. Appendix

A.1. Manual of the FEM-program

The FEM algorithm to solve 2D heat conduction problems numerically was written in MATLAB. First of all the basic domain Ω has to be defined and prepared for the main program main.m, which is done by the routines triangulation.m and PET_output.m

Definition and Preparation of the Basic Domain:

- The routine triangulation.m is opened.

- The basic domain Ω is defined by a closed polygon. It is described by the points $P_i = (\text{xpoints}_i, \text{ypoints}_i)$.

- The vector for the x-coordinates is defined: xpoints$= [x_1, ..., x_n]$.

- The vector for the y-coordinates is defined: ypoints$= [y_1, ..., y_n]$.

- The MATLAB-routine pdepoly(xpoints,ypoints) is called to create the polygon surface.

A pdetool-window of the pdetoolbox from the MATLAB-program system is opened where the basic domain is shown. The triangulation of the polygon surface is done in this window in the following way:

- Mesh$\longrightarrow$Initialize Mesh...A first triangulation of the surface is done.

- Mesh$\longrightarrow$Refine Mesh...The mesh of the surface gets finer.

- Mesh$\longrightarrow$Show Node Labels...The labels of the points are shown.

- Mesh$\longrightarrow$Export Mesh...All parameters used for the FEM-algorithm are exported.

- A window "p e t" opens$\longrightarrow$Press "OK" and then "Exit".

- A small window opens, asking you to save the generated basic domain and the triangulation pattern as a MATLAB-script⟶By pressing "No" the pde-window closes.

In the MATLAB-window, the routine PET_output.m has started to write all relevant data in separate ASCII-files in a specific format:

- number.txt...vector with the number of triangles, number of points and number of edges

- points.txt...x- and y-coordinates of all points

- edges.txt...point labels of the boundary counterclockwise

- triangles.txt...point labels of the triangles

The Main Routine main.m:
In the main program main.m, the FEM-algorithm to solve heat conduction problems in 2D is programmed. At first the four ASCII-files from above are loaded. Next the parts of the boundary are assigned to Dirichlet, Cauchy or Neumann boundary conditions respectively:

- n0=load('number.txt')

- p0=load('points.txt')

- e0=load('edges.txt')

- t0=load('triangles.txt')

- ed...point labels for Dirichlet boundary conditions

- ec...point labels for Cauchy boundary conditions

- en...point labels for Neumann boundary conditions

Now the parameters and functions for the specific problem of the cooling process of the copper string are shown. The following important parameters are used:

l0	length of the copper string in m
t1	thickness of the copper string in cm
dt	time step in s
iter	number of iterations for the time evolution
str	string expression for the saving data file
Tstuetz	observed temperature point in K
Tw	temperature of the vacuum walls in K
Tanf	initial temperature of the copper string in K
kappa	product of density and specific heat capacity of copper $\mathrm{Jcm^{-3}K^{-1}}$
landa	heat conductivity of copper in $\mathrm{Wcm^{-1}K^{-1}}$
astr(T)	radiation coefficient dependent on the temperature
qpK(T)	thermal flow density dependent on the temperature
astrp(T)	derivative of the radiation coefficient dependent on the temperature
qpKp(T)	derivative of the thermal flow density dependent on the temperature

The following functions were used during the calculation:

triangles.m	contributions of the triangles to the LES
topnlin.m	contributions of the top surface to the LES
cauchynlin.m	contributions of the Cauchy boundary conditions to the LES
neumannnlin.m	contributions of the Neumann boundary conditions to the LES

For the simulation a grid of points is defined over the basic domain and a simple interpolation is used to calculate the temperatures at these points. At first it has to be determined to which triangle the points belong. The output consists of the actual time and the actual temperature at the observed temperature point. Also an animation of the cooling process of the copper string is done.

A.2. Manual of the CC-program from Dr. A. Kaufhold

In 1996 Dr. A. Kaufhold has written a CC-program in TURBO-PASCAL based on the predictor-corrector Numerov algorithm. However, nowadays computer processors are much faster and thus the routines have to be patched first. The program is normally started in MS-DOS, therefore a DOS emulator (e.g. DOSBOX) is used. Also a virtual disc drive for the output has to be created. When the program ImDisk Virtual Disk Driver is started, the following steps are taken:

- Press "Mount New"...$\longrightarrow$A "Mount new virtual disk" window opens.

- Choose a "Drive letter" (e.g. E).

- Choose a "Size of virtual disk" (e.g. 1024 Kilobytes), the unit is chosen with a radio button.

- Choose a "Device type" (e.g. Floppy).

- Press "OK"$\longrightarrow$A virtual memory of size 1 MB with the drive letter E: is created.

- A window opens where you are asked to format the data medium$\longrightarrow$Press "Datenträger formatieren".

- A window "Wechseldatenträger (E:) formatieren" opens$\longrightarrow$Press "Starten".

- Press "OK" in the warning.

- Press "OK" in the info "Formatieren abgeschlossen".

- Close the window "Wechseldatenträger (E:) formatieren".

Next the DOSBOX is started and the following procedure takes place before the CC-program can be executed:

- Type in mount e e: -t floppy...mounting of the virtual disk drive.

- Type in mount c c:...mounting of the local drive.

- Type in c:...change to drive c.

- Type in cd CC...change the directory where the exe-file of the CC-program is.

Before the CC-program is started, the following Inputfiles have to be modified. The interaction potential is chosen to be a Lennard-Jones-Devonshire Potential and defined in the Inputfile potential.001:

a	stiffnessparameter in Å^{-1}
e0	well depth in eV
z0	equilibrium distance in Å
gamma_1	damping coefficient for surface vibrations

The structure of the crystal surface is defined in the file surface.001:

a1	length of the first lattice vector in Å
a2	length of the second lattice vector in Å
alpha	angle between a1 and x-axis in degrees
beta	angle between a2 and x-axis in degrees
ts	surface temperature in K
ár_10	1st order corrugation in x-direction
ár_01	1st order corrugation in y-direction

The following initial conditions of the helium atoms are defined in the Inputfile particle.001:

total mass in g/mol
incident wavevector in Å^{-1}
polar angle in degrees
azimuthal angle in degrees

The numerical integration parameters are defined in integrate.001:

number of steps for Gram-Schmidt orthogonalisation
initial step size for the numerical integration
integration procedure accuracy
energy threshold for zstart calculation

In the file basic.001, the energy threshold is chosen first and then the basis set of channels is defined. In the DOSBOX-window, nummain.exe is typed to start the CC-program. The procedure for simple elastic HAS calculations is as follows:

- Pure Close Coupling Calculations? (Y/N) : y

- Numerical Integrated Coupling Calculations? (Y/N) : n

- Input Data Files: potential.001, surface.001, particle.001, integration.001

- Systematic Study? (Y/N) : n

- Filename of Inputfile: basic.001

At first the coupling matrix for the included channels is calculated. Then the output channels are listed with decreasing energy and the numerical integration is started. The output parameters are given in the table of State Transition Probabilities:

i	channel number
(G, j, v)	reciprocal lattice vector, rotational quantum numbers
	vibrational quantum number
ϕf[°]	polar angle
θf[°]	azimuthal angle
Ez[meV]	energies in z-direction
v[m/s]	particle velocity
RE_SMAT	real part of the scattering vector
IM_SMAT	imaginary part of the scattering vector
P(i,f)	scattering probability

Also the symmetry direction, the number of integration steps, the occupation of the scattering matrix in %, the total computing time in s and the number of channels is given. The sum of the scattering probabilities is approximately 1 for a good calculation. By typing the number 6, the Close Coupling program is closed.

A.3. Manual of the self-written CC-program

The program main.m written in MATLAB computes the scattering intensities of helium atoms, which are scattered elastically from crystal surfaces. The calculation is done by the Coupling-Channel method originally proposed by Liebsch and Harris. The interaction potential is a corrugated Morse potential. At first natural units are chosen:

m	particle mass in kg
e0	elementary charge in C
hquer	plancks reduced constant in Js
L0	length scale
E0	energy scale

Then the initial conditions for the helium atoms are defined:

thetai	incident angle in degrees
ki	incident wavevector in $\mathrm{\AA}^{-1}$

Also the surface structure has to be determined:

a1	length of the basis vector a1 in $\mathrm{\AA}$
a2	length of the basis vector a2 in $\mathrm{\AA}$
alpha1	angle enclosed by a1 and the x-axis
alpha2	angle enclosed by a2 and the x-axis

The parameters of the Morse corrugated potential is defined in the following way:

D0	well depth in meV
chi	stiffness parameter in $\mathrm{\AA}^{-1}$
h	corrugation amplitude
basis	basisset of Gmn-vectors (load('basisset.txt'))
fourier	basis for the Fourier series of the interaction potential (load('fourier.txt'))
fun0	function for the Fourier coefficients
xi	surface shape function in $\mathrm{\AA}$

For the coupling channel method, certain parameters have to be defined:

hi	step width on the left hand side in Å
hM	step width on the right hand side in Å
gammai	arbitrary small number on the left hand side
gammaM	arbitrary small number on the right hand side
ze	matching point in Å
zmi	initial point on the left hand side in Å
zmM	initial point on the right hand side in Å
Eth	threshold energy in meV

The routine basisset.m chooses the channels with energies above the threshold energy from the variable basis and lists them with decreasing energies. The routine coupling.m performs the numerical integration and calculates the scattering probabilities for the different channels. The first two columns of the output correspond to the different channels and the third one corresponds to the scattering probabilities. For a good calculation, the sum of the scattering probabilities is equal to 1.